Computer Physics Communications 321 (2026) 109998

Contents lists available at ScienceDirect

Computer Physics Communications

journal homepage: www.elsevier.com/locate/cpc

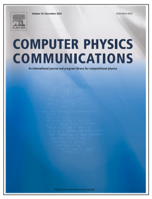

Computational Physics

Benchmarking Monte Carlo codes for the modelling of low-energy neutron production target reactions

Sherryn MacLeod [a,b], Klaudiusz Jakubowski [b], James Vohradsky [a], Daniel R. Franklin [c], Toshiro Sakabe [d], Akram Hamato [e], Masahiro Okamura [d], Susanna Guatelli [a], Mitra Safavi-Naeini [b,*]

[a] Centre for Medical Radiation Physics, University of Wollongong, Wollongong, 2522, NSW, Australia
[b] Australian Nuclear Science and Technology Organisation, Lucas Heights, Sydney, 2234, NSW, Australia
[c] School of Electrical and Data Engineering, University of Technology Sydney, Sydney, 2007, NSW, Australia
[d] Brookhaven National Laboratory, Upton, NY, 11973, USA
[e] National Institutes for Quantum Science and Technology, Chiba-shi, 263-8555, Japan

ARTICLE INFO

The review of this paper was arranged by Prof. Z. Was

Keywords:
Accelerator based neutron source
Monte Carlo
Geant4
FLUKA
PHITS
MCNP
BNCT
Target optimisation

ABSTRACT

The increasing adoption of accelerator-based neutron sources (ABNS) for applications including neutron capture therapy (NCT) research has highlighted the need for accurate simulation tools. Precise modelling of the neutron production target is crucial to ensure that simulated predictions of neutron beam characteristics used for subsequent beam shaping assembly design are reliable. This work presents a comprehensive benchmarking of four widely-used Monte Carlo codes - Geant4, PHITS, FLUKA (CERN), and MCNP - for modelling low-energy neutron production target reactions. Using their recommended physics models and cross-section libraries, we evaluate each code's performance in simulating four beam-target reactions: ^{7}Li(p,n)^{7}Be, ^{9}Be(p,n)^{9}B, ^{9}Be(d,n)^{10}B, and C(d,n)N. Predictions of neutron yield, angular distributions, and energy spectra are compared against available thick target experimental data. Results show varying levels of agreement between the codes depending on the reaction type, energy range, and beam characteristics. Geant4, MCNP and PHITS are the overall best performing codes for the simulation of total neutron yield and yield in the forward direction across most reactions. Across energies where experimental benchmarks exist, inter-code discrepancies in total and forward-directed yield are typically 10 to 30%, with larger deviations at near-threshold incident ion energies. PHITS provides the best overall reproduction of experimental spectra, particularly for the ^{9}Be(p,n)^{9}B reaction. Additionally, PHITS demonstrates superior computational performance for most reactions. These findings provide valuable guidance for ABNS design, highlighting the strengths and limitations of each code for the simulation of low-energy neutron production reactions .

1. Introduction

The development of accelerator-based neutron sources (ABNSs) has gained momentum in recent years. This shift is largely driven by the high costs, substantial physical footprint, and complex safety and security requirements of nuclear research reactors, which have limited their accessibility for many industrial and medical use cases [1]. ABNSs support a wide variety of applications, including neutron imaging and radiography [2,3], astrophysics research [4,5], isotope production [6,7], and nuclear data measurements [8]. ABNSs have also become increasingly important for expanding the availability of medical applications such as neutron capture therapy (NCT), since they are now the most practical and cost-effective method for producing the required neutron fluences and spectra [9].

An ABNS consists of three main components: the accelerator, the neutron production target, and the beam shaping assembly (BSA) (Fig. 1). A neutron beam suitable for NCT applications requires high neutron flux ($\geq 10^{9}$ n/cm^{2}/s), with thermal energies ($E \leq 0.5$ eV) present at the tumour site [10]. To achieve this, an epithermal neutron beam (0.5 eV< E < 10 keV) exiting the BSA is required [11].

The design and optimisation of the BSA such that it can be used to produce a beam conforming to these requirements is greatly influenced

---

* Corresponding author .

E-mail addresses: sjm842@uowmail.edu.au (S. MacLeod), jakubowk@ansto.gov.au (K. Jakubowski), jamesv@uow.edu.au (J. Vohradsky), daniel.franklin@uts.edu.au (D.R. Franklin), tsakabe1@bnl.gov (T. Sakabe), mohammadi.akram@qst.go.jp (A. Hamato), okamura@bnl.gov (M. Okamura), susanna@uow.edu.au (S. Guatelli), mitras@ansto.gov.au (M. Safavi-Naeini).

https://doi.org/10.1016/j.cpc.2025.109998
Received 11 March 2025; Received in revised form 23 November 2025; Accepted 12 December 2025

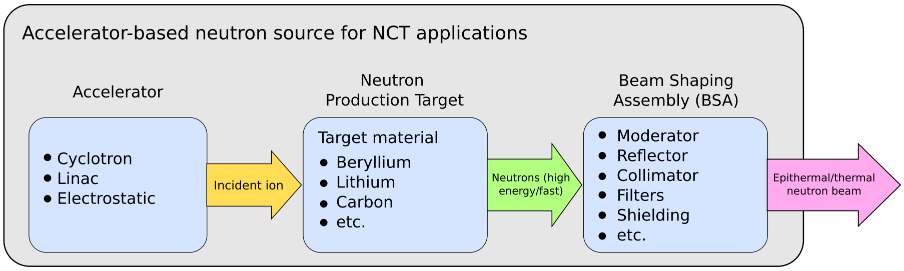

Fig. 1. A simplified schematic diagram of an accelerator-based neutron source for NCT applications. Adapted from Kumada et al. [11].

Table 1
Properties of different low-energy reactions for accelerator based neutron sources. Information present in this table is from Cartelli et al. [12] unless otherwise specified.

Reaction	Threshold energy (MeV)	Q-value (MeV)	Target melting point (°C)	Thermal conductivity (W/(m K))	Radioactive products	Notes
^{7}Li(p,n)^{7}Be	1.88	−1.65	180	84.7	Yes, ^{7}Be[a]	**Advantages** • High neutron yield [17] • Soft neutron spectrum close to the threshold energy [18–20] **Disadvantages** • Heat load challenges due to poor material properties [12,21] • Li is unstable in air and produces radioactive byproducts [22–24]
^{9}Be(p,n)^{9}B	2.06	−1.85	1287	201	No	**Advantages** • Remains stable under high heat loads and easier to handle (relative to ^{7}Li target) [25] **Disadvantages** • Lower neutron yield than ^{7}Li target • Requires larger accelerator systems and more extensive moderation [26]
^{9}Be(d,n)^{10}B	0, 0.916[b]	4.26 [15]	1287	201	No	**Advantages** • Exothermic, neutron yields comparable to proton-induced reactions at low incident energies [15] **Disadvantages** • Fast neutron production
^{13}C(d,n)^{14}N ^{12}C(d,n)^{13}N[c]	0, 0	5.33, -0.28 [27,28]	3550	230	No	**Advantages** • Carbon is a very stable material with excellent thermal properties [29] • Potential for smaller accelerator designs **Disadvantages** • Fast neutron production

[a] ^{7}Be $T_{\frac{1}{2}} = 53.2$ days.

[b] Three closely spaced excited levels in the residual ^{10}B nucleus (N6, N7, N8, at 5.11, 5.16, 5.18 MeV respectively) are preferentially populated [30].

[c] Natural abundance of ^{13}C is ~1% (99% ^{12}C) [31].

by the choice of neutron production target reaction. This reaction determines the source efficiency, and the collimation, moderation and shielding needed to achieve a neutron beam with the desired spatial, spectral and fluence characteristics. For NCT applications, reactions driven by low-energy bombarding ions are preferred as they limit the fast neutron component of the resulting predominantly epithermal neutron beams. This approach not only minimises shielding requirements but also minimises neutron activation [12].

Out of the numerous low-energy neutron production reactions available, only a few have been seriously considered for ABNS target design due to radiation safety concerns, neutron production efficiency, and practical considerations [13,14]. The most commonly used reactions are ^{7}Li(p,n)^{7}Be and ^{9}Be(p,n)^{9}B, with the less common ^{9}Be(d,n)^{10}B and ^{13}C(d,n)^{14}N reactions also under investigation [15,16]. Table 1 summarises the main reactions which have been proposed for use in ABNSs.

Simulation using Monte Carlo (MC) particle transport codes has become integral to ABNS target and BSA design. These codes provide a quick and effective solution for system design and evaluation, attracting users with varying levels of expertise. However, precise and accurate modelling of the target and neutron production is critical to ensure that simulated predictions regarding neutron spectrum, yield and shielding requirements for subsequent BSA design are valid.

The aim of this paper is to provide a quantitative review and benchmark of four widely used MC codes - Geant4, PHITS, FLUKA (CERN) and MCNP - for simulating low-energy neutron production target reactions proposed for use in ABNS, particularly for NCT applications. Each code's performance in modelling neutron yield, angular distributions and energy spectra is evaluated for the following key reactions: ^{7}Li(p,n)^{7}Be, ^{9}Be(p,n)^{9}B, ^{9}Be(d,n)^{10}B, and C(d,n)N. The objective is to assess the capabilities of each code using their respective developer recommended configuration of physics settings, with no adjustments made to the source code or substitution of nuclear data. This will provide valuable insight into the accuracy, and computational speed for designing ABNS systems, especially in the low-energy range critical for NCT applications.

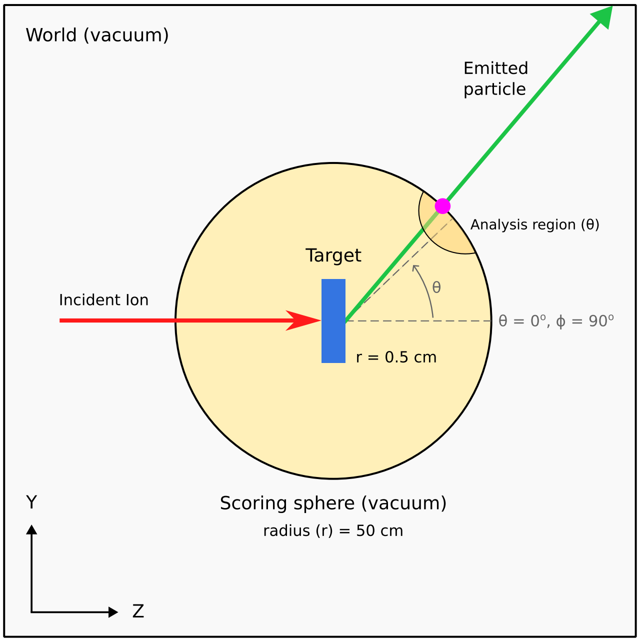

Fig. 2. A schematic of the simulation geometry used across all Monte Carlo codes for each reaction. An ideal beam is incident on a cylindrical target with radius $r = 0.5$ cm and thickness selected based on the expected maximum penetration depth plus a margin of 50%. The type, energy, and position of the emitted particles are scored at the boundary crossing of the surrounding scoring sphere. For yield metrics with angular dependence, calculations are performed within an analysis region defined using azimuthal angle $\phi = 90^\circ$, and polar angle $\theta \in [0, 180^\circ]$ (i.e. in the YZ plane, with $\theta = 0^\circ$ being parallel with beam direction).

2. Monte Carlo transport codes, models and data libraries

The four Monte Carlo codes evaluated for modelling low-energy target reactions for ABNS in this study are:

- The GEometry ANd Tracking simulation toolkit (Geant4): An open-source C + + MC toolkit, developed by a large collaboration based at CERN, Geneva, Switzerland, now widely used in medical physics and capable of handling complex geometries [32,33];
- Monte Carlo N-Particle (MCNP) MCNP: Developed by the Los Alamos National Laboratory, New Mexico, USA, highly regarded for its neutron transport capabilities [34,35];
- Particle and Heavy Ion Transport Code System (PHITS): A general-purpose MC code developed through collaboration between several Japanese institutes, capable of modelling most particle transports up to 1 TeV [36]; and
- CERN[1] FLUKA (FLUktuierende KAskade in German, i.e., fluctuating cascade): Originally used for high-energy physics, has gained popularity for low-energy applications [37,38].

These codes are all widely used in the field and offer a variety of different approaches to particle transport simulation. Geant4 utilises a C + + object-oriented architecture with a macro scripting language, and is distributed under a permissive open-source license, offering significant flexibility for developers and commercial users. In contrast, PHITS, FLUKA (CERN) and MCNP are primarily Fortran-based, with each code being closed-source or restricted-source (with the exception of those at developer organisations or who have obtained explicit approval). These codes offer a degree of flexibility for their intended use cases through card (command)-based text input. A comparative summary of the features of these MC codes is provided in Table 2.

2.1. Simulation parameters, selected models and data libraries

In this study, each Monte Carlo code was configured using the recommended[2] or most appropriate physics and models/data libraries available to the user for low-energy light-ion neutron production reactions, without applying advanced adjustments to the source code or importing external cross-section datasets, unless otherwise specified. When available, thermal neutron scattering libraries were used for neutron transport within target materials. The following subsections go into detail about the cross-section data libraries and nuclear interaction models are provided in the following subsections, with a summary presented in Table 3.

2.1.1. GEANT4

Geant4 version 11.1.3 was used in this study[3] [32]. The QGSP_BIC_AllHP physics model list was used;[4] it includes the All High Precision (AllHP) model which uses TALYS-based Evaluated Nuclear Data Library (TENDL) cross-sections for alpha, deuterons, ^{3}He, protons, and tritons below energies of 200 MeV. The TENDL database is composed of calculated results using the TALYS nuclear model code [39], with some simulated results overruled by high-quality experimental

---

[1] *Note:* there are two distinct FLUKA versions distributed by joint copyright owners CERN and INFN; in this work, we use FLUKA (CERN) exclusively.

[2] Recommended physics settings were taken from each code's official user manual or documentation: Geant4 - *Manual For Application Developers*, Version 11.1 and *Physics List Guide*, Version 11.1; PHITS - *PHITS User Manual*, Version 3.33; FLUKA - *FLUKA Manual*, Version 4-4.0; MCNP - *MCNP Theory & User Manual*, Code Version 6.3.0, Los Alamos National Laboratory Report LA-UR-22-30006.

[3] 11.2.0, 11.2.1 and 11.2.2 have since been released, however due to some unexpected behaviour in neutron yield in these releases they were not used in this study; results are included in Supplementary Materials Section S2.1

[4] The QGSP_BIC_HP physics list can also be used for neutron interactions. A comparison between both the QGSP_BIC_AllHP and QGSP_BIC_HP physics lists (as of Geant4 version 11.1.3) and justification for why QGSP_BIC_AllHP has been used is included in Supplementary Materials Section S2.1.

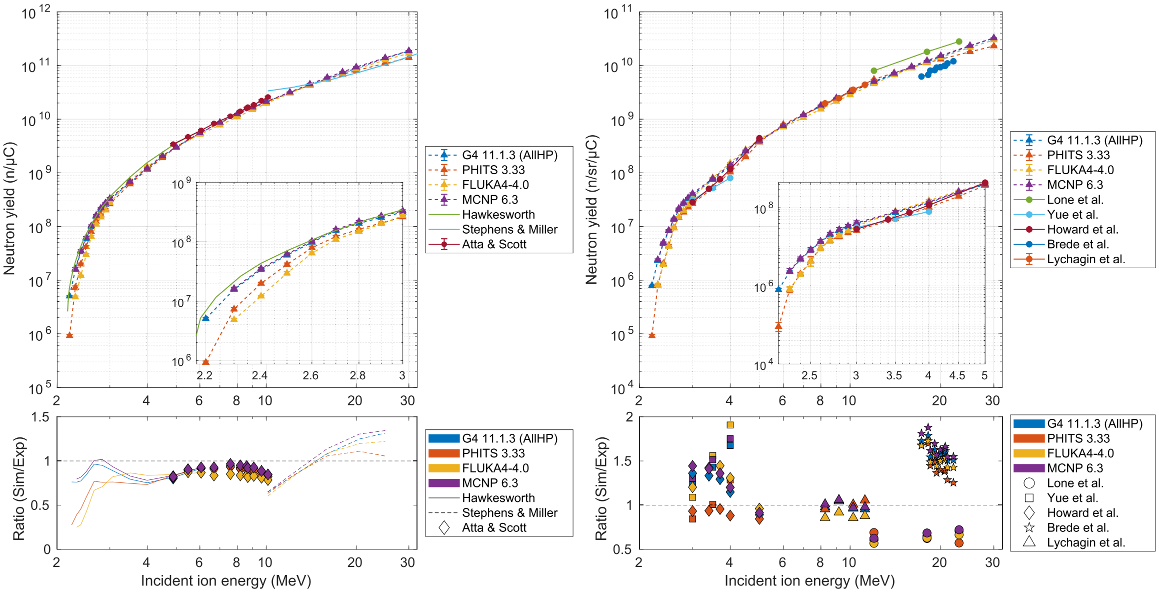

(a) Total yield (b) Yield at 0°

Fig. 3. Neutron yield for the ^{9}Be(p,n)^{9}B reaction from incident proton energies of 2.2 MeV to 30 MeV. (a) Total neutron yield from each MC code compared to reference data from Atta and Scott [52], Hawkesworth [50] and Stephens and Miller [51]. (b) Neutron yield in the forward direction ($\theta = 0°$) from each code is compared to reference data from Lone et al. [57], Yue et al. [54], Howard et al. [55], Brede et al. [56] and Lychagin et al. [53].

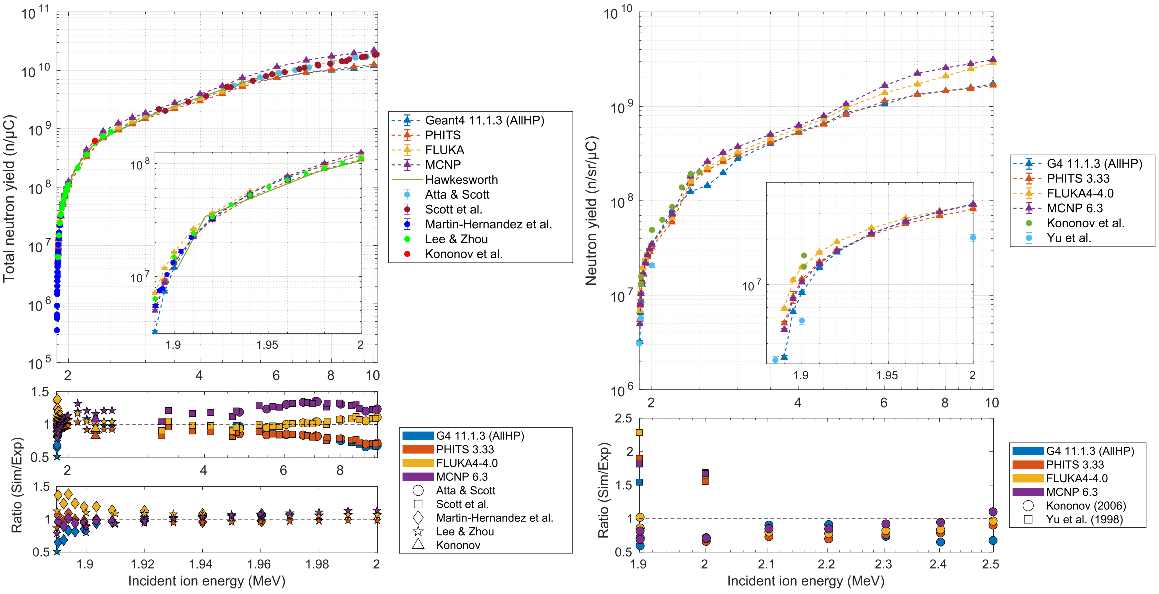

(a) Total yield (b) Yield at 0°

Fig. 4. Neutron yield for the ^{7}Li(p,n)^{7}Be reaction from incident proton energies of 1.89 MeV to 10 MeV. (a) Total neutron yield from each MC code compared to reference data from Hawkesworth [50], Atta and Scott [52], Scott [59], Martín-Hernández et al. [58], Lee and Zhou [60] and Kononov et al. [61]. (b) Neutron yield in the forward direction ($\theta = 0°$) from each code is compared to reference data from Kononov et al. [61] and Yu et al. [62].

data where possible [40]. For target materials ^{9}Be and ^{7}Li in Geant4, proton cross-section data from ENDF/B-VIII.0 has been inserted into the TENDL dataset up to 113 MeV and 10 MeV, respectively. Geant4's deuteron interaction cross sections for ^{9}Be, ^{7}Li, ^{6}Li, ^{12}C and ^{13}C are taken from the JENDL/DEU-2020 data library up to 200 MeV [41], while default neutron ($E_n < 20$ MeV) cross-section data and final states are obtained from JEFF-3.3 [42]. Thermal scattering data is obtained from JEFF-3.3, supplemented with ENDF/BVIII-0 for materials not included within JEFF-3.3. Below 10 GeV, heavy ions are transported using the Binary Cascade model.

2.1.2. PHITS

PHITS (version 3.33 [36]) utilises the JENDL-4 database for neutron transport below 20 MeV. For proton interaction cross sections, it is recommended by Sato et al. [36] that the JENDL-5 evaluated data library is used (INCL4.6 is used by default) [43]. In addition, the JENDL-5 sublibrary for deuterons is included, which is primarily based on JENDL/DEU-2020. To describe thermal neutron transport, the thermal scattering library (based on JENDL-4) is applied to the target material when needed. Heavy ion transport in PHITS uses the INCL model below 10 MeV/n.

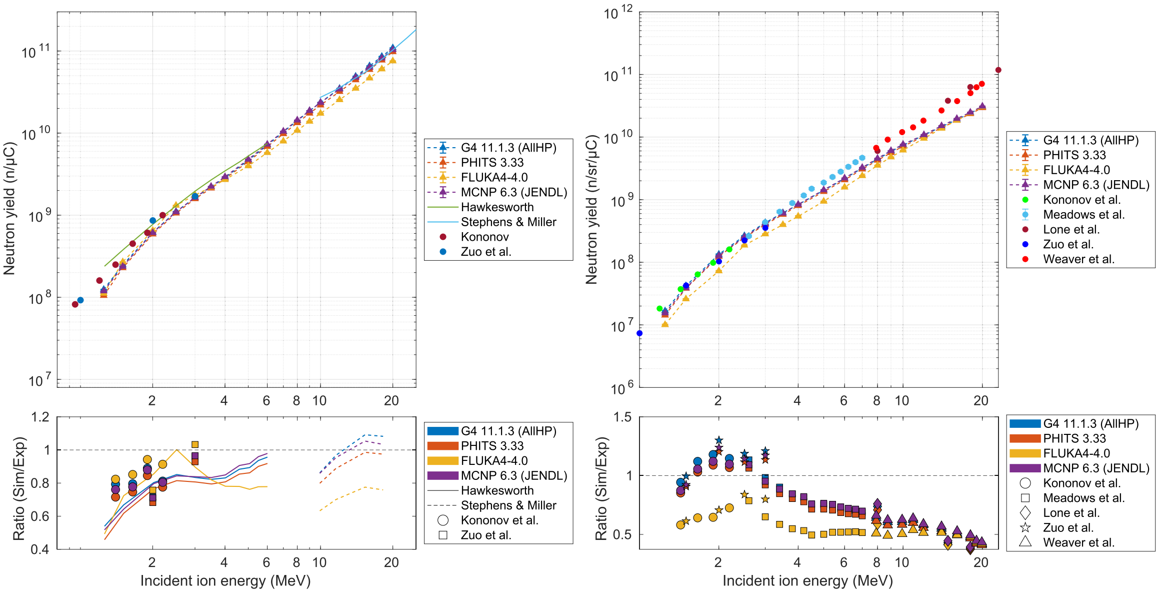

(a) Total yield (b) Yield at 0°

Fig. 5. Neutron yield for the ^{9}Be(d,n)^{10}B reaction from incident deuteron energies of 1.25 MeV to 20 MeV. (a) Total neutron yield from each MC code compared to reference data from Hawkesworth [50], Stephens and Miller [51], Kononov et al. [61], and Zuo et al. [63]. (b) Neutron yield in the forward direction ($\theta = 0°$) from each code is compared to reference data from Kononov et al. [61], Meadows [64], Lone et al. [57], Zuo et al. [63], and Weaver et al. [65]. The data shown from Weaver et al. is for $\theta = 3.5°$.

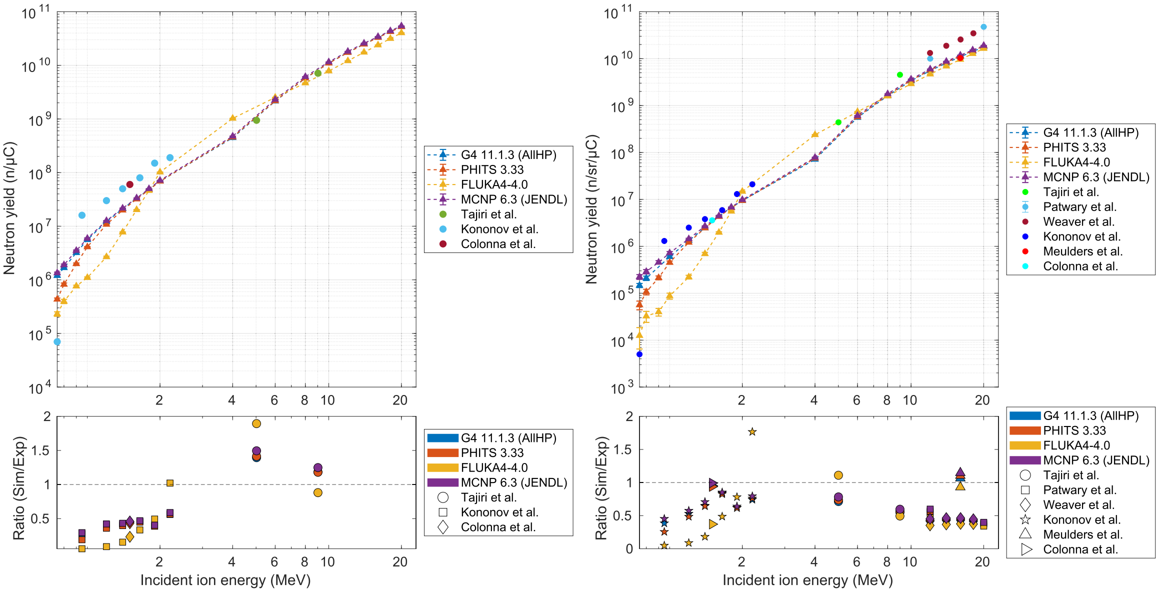

(a) Total yield (b) Yield at 0°

Fig. 6. Neutron yield for the C(d,n)N reaction from incident deuteron energies of 0.75 MeV to 20 MeV. (a) Total neutron yield from each MC code compared to reference data from Tajiri et al. [66], Kononov et al. [61], and Colonna et al. [67]. (b) Neutron yield in the forward direction ($\theta = 0°$) from each code is compared to additional reference data from Patwary et al. [68], Meulders et al. [69], and Weaver et al. [65]. The data shown from Weaver et al. is for $\theta = 3.°$.

2.1.3. *FLUKA (CERN)*

FLUKA (CERN) version 4-4.0 has been used in this work [37]. The DEFAULT card in FLUKA was set to “PRECISIOn” where the hadronic interactions are handled by FLUKA’s hadron-nucleus nuclear interaction model, PEANUT (PreEquilibrium Approach to Nuclear Thermalisation). For simulation of deuterons, “LOWDEU” was activated using the PHYSICS card to use the low-energy deuteron nuclear interaction model. Point-wise neutron interactions below 20 MeV energy are handled by the JEFF-3.3 (default) neutron data library [42].

2.1.4. *MCNP*

MCNP version 6.3 was used for this study [35]. Proton cross section data was taken from the ENDF70PROT library based on ENDF/B-VII.0 [44]. Note that proton-induced interactions in ENDF/B-VIII.0 (used in Geant4) were carried over from ENDF/B-VII.0 with minor corrections, and as such, they contain almost identical cross-section data. For ^{9}Be, the “Be-9 endf70prot” errata was added. The chosen nuclear model is “Bertini INC”. The ENDF71x (293.6 K) continuous-energy data library based on ENDF/B-VII.1 [45,46] was used for the simulation of neutron

Table 2
Comparison of Geant4, PHITS, FLUKA, and MCNP.

	Geant4	PHITS	FLUKA (CERN)	MCNP
Availability and licensing	Permissive Open Source (Geant4 Software License)	Requires approval; source code available for academic use under institutional licenses, subject to export controls, no redistribution	FLUKA Licence; source code available for CERN staff and affiliates of institutes with an Institutional FLUKA Licence, no redistribution	RSICC Single User Licence - Closed Source (source code available to US citizens only, no redistribution)
Language	C++	Fortran	Fortran 77	Fortran, C, C++
Input	C++ application + macro scripts	Card based text input	Card based text input	Card based text input
Graphical user interface and visualisation	Visualisation and GUIs available, multiple toolkits including Qt and Vtk	Visualisation available	Flair (input & visualisation)	Tally plotter available
Multi-threading	Yes	Yes (OpenMP)	No	Yes (OpenMP, MPI)
Scoring	Custom + primitive scorers	Built in (can create custom tallies)	Built in (can create custom routines)	Built in (can create custom tallies)
Active user forum	Yes	Yes	Yes (invite only)	Yes (by request)

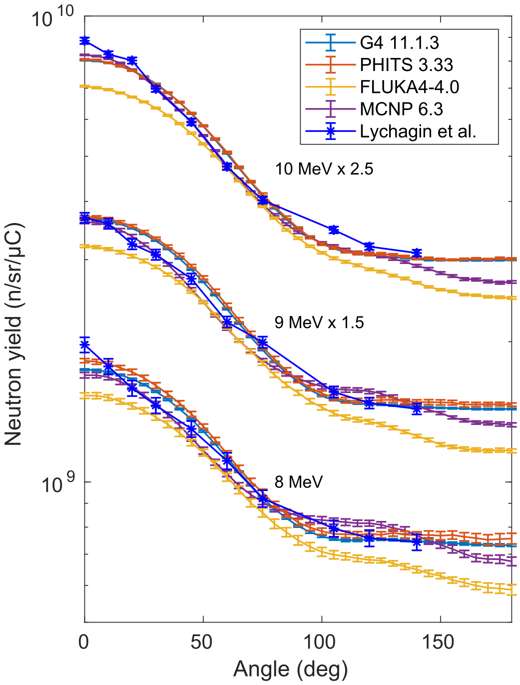

Fig. 7. Angular distribution (with respect to beam direction) of the neutron yield for the ^{9}Be(p,n)^{9}B reaction with incident ion energy of 8 MeV, 9 MeV, and 10 MeV compared to reference data from Lychagin et al. [53] at 8.26 MeV, 9.18 MeV and 10.24 MeV respectively. Curves labelled "10 MeV × 2.5" and "9 MeV × 1.5" have been scaled by factors of 2.5 and 1.5, respectively for visual clarity.

interactions along with thermal scattering data tables from ENDF71SaB based on ENDF/B-VII [47]. It is important to note that MCNP does not have a dedicated nuclear data library for deuterons incident on ^{9}Be and ^{12}C/^{13}C targets. As such, both the dedicated model that handles light ion interactions, ISABEL, and JENDL/DEU-2020 ACE files added to the cross-section directory in MCNP were evaluated. As shown in Supplementary Material Section S2.2, MCNP's ISABEL model is not able to simulate neutron production from deuteron interactions below ~6 MeV. Therefore, JENDL/DEU-2020 ACE files have been used for benchmarking purposes.

3. Methods

A set of equivalent simulations featuring identical physical geometry, particle beam characteristics, target compositions and scoring methods are implemented across each of the four simulation codes. A simplified and consistent geometry was adopted across all codes to facilitate inter-code comparison under controlled conditions. This geometry approximates, but does not replicate, typical experimental target setups, with only the target material, thickness and incident ion energy varied per reaction. For each ABNS reaction, the results were analysed using a range of metrics to evaluate the total neutron yield and the spectral and angular distribution of neutrons predicted by each code. Additionally, the single-threaded computational performance of each of the codes is evaluated and compared.

To assess the performance of each code for modelling low-energy neutron production reactions, available experimental datasets reporting thick target yields (TTY) have been collated for comparison with simulation results. These datasets were selected prior to simulation and analysis based on their alignment with the scope of this study. The scope was defined by the incident ion species, the incident ion energy ranges and the target materials considered. For comparison with simulation results, datasets with experimental results presented in comparable yield units, and with the same (or very similar) incident ion energies as those simulated for angular and spectral distributions, were selected. Datasets that did not meet these criteria, or which lacked sufficient data points, were excluded. This data has been compiled using entries present in the EXFOR database [48,49] and an independent literature review. A list of experimental data that has been collated during this study, along with relevant information about the TTY, can be found in Supplementary Material Section S2.4.

3.1. Simulation geometry and materials

The simulation geometry, contained within a 2.5 m cubic vacuum world, is illustrated in Fig. 2. This simplified, standardised geometry can be reproduced identically in all Monte Carlo codes benchmarked, is generic enough to represent the range of experimental set-ups used to produce benchmarking data for the reactions of interest, and allows for the isolation of differences stemming from code-dependent physics models and cross-section datasets. The beam is aligned with the Z axis of the coordinate system (beam direction positive); the Y axis is vertical (up positive). Spherical angles follow the physics convention, with θ being the polar angle and ϕ being the azimuthal angle.

Identical geometry, materials (Table 4) and particle source components of the target system were simulated across all codes.

The ion source is modelled as a perfectly-collimated zero-width pencil beam of the selected ion species emitted from a point at (0, 0, −2) m travelling in the positive Z-axis direction.

The cylindrical target has a radius of 0.5 cm, sufficient to encapsulate the lateral width of the interaction volume for 30 MeV protons on a beryllium target, which represents the scenario with the most significant lateral scattering.

The target thickness for each reaction was determined by simulating 10^{4} incident ions for each reaction-energy combination in

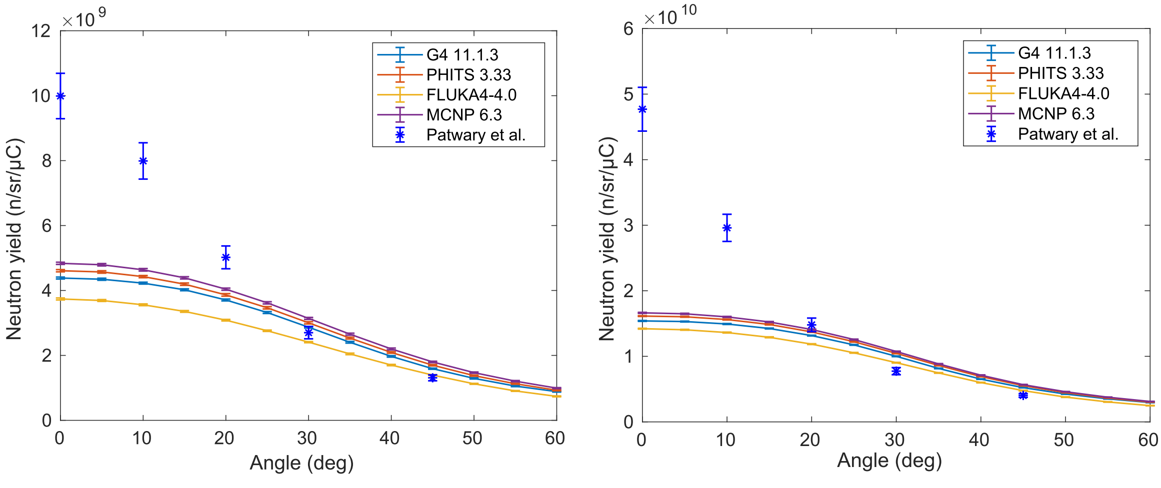

(a) 12 MeV (b) 20 MeV

Fig. 8. Angular distribution of the C(d,n)N reaction with incident deuterons of (a) 12 MeV and (b) 20 MeV compared to results by Patwary et al. [68].

Table 3
Details of cross section data libraries and models for particle transport used in each Monte Carlo code.

Physics option	Geant4 11.1.3 QGSP_BIC_AllHP	PHITS 3.33 –	FLUKA 4-4.0 DEFAULT card: PRECISIOn	MCNP 6.3 –
Protons	< 6 GeV; Binary Cascade, < 200 MeV; ParticleHP (G4TENDL) **Data libraries:** TENDL-2019, ENDF/B-VII.0	< 200 MeV; JENDL-5 (INCL4.6 default), < 1 MeV; INCL4.6	< 5 GeV/c; PEANUT model	< 113 MeV; endf70prot **Data libraries:** ENDF/B-VII.0
Deuterons	< 6 GeV/n; Binary Cascade, < 200 MeV/n; ParticleHP (G4TENDL) **Data libraries:** TENDL-2019, JENDL/DEU-2020	< 200 MeV/n; JENDL-5 (for selected isotopes, INCL4.6 default), < 1 MeV/n; INCL4.6 (JENDL-5 can be forced below this energy)	< 150 MeV/n; low-energy deuteron nuclear interaction model	< 940 MeV/n; ISABEL (default) **Added ACE files:** JENDL/DEU-2020
Heavy ions	< 10 GeV; Binary Cascade	< 3 GeV/n; JQMD + GEM < 10 MeV/n; INCL4.6	< 5 GeV/n; RQMD, Boltzmann Master Equation	LAQSM03.03
Neutrons	> 20 MeV; Binary cascade < 20 MeV; NeutronHP (G4NDL) **Data libraries:** JEFF-3.3	< 200 MeV; JENDL-5 (INCL4.6 default), < 20 MeV; JENDL-4	> 20 MeV; PEANUT model, < 20 MeV; JEFF-3.3 (default)	< 20 MeV; endf71x **Data libraries:** ENDF/B-VII.1
Thermal Scattering	< 4 eV; NeutronHP Thermal Scattering **Data libraries:** JEFF-3.3, ENDF/BVIII-0	JENDL-4 TSL	JEFF-3.3	ENDF/B-VII.1

Table 4
A summary of the target materials used for each reaction across all codes.

Target material	Relevant reactions	Composition	Density (g/cm^3)
Be	^{9}Be(p,n)^{9}B, ^{9}Be(d,n)^{10}B	^{9}Be	1.850
Li	^{7}Li(p,n)^{7}Be	^{7}Li	0.534
C	C(d,n)N	^{nat}C (99% ^{12}C, 1% ^{13}C)	2.260

Geant4 11.1.3, then multiplying the maximum penetration depth by 1.5. The 50% post-Bragg peak margin ensures that all incident ions will be stopped by the target, while minimising neutron moderation in the target itself. A comparison of the generated and exiting neutron spectra for low and high incident ion energy cases was performed for each reaction to ensure that this margin did not introduce significant neutron moderation (see Supplementary Material S1.2). Although this simulation model is not identical to all of the reference experimental configurations described in the literature, it is broadly representative of the typical geometry used in these studies.

A vacuum scoring sphere with a radius of 50 cm surrounds the target, recording the particle type, energy, and position at its boundary. The centre of the scoring sphere was co-located with the geometric centre of the target.

Reactions ^{7}Li(p,n)^{7}Be, ^{9}Be(p,n)^{9}B, and ^{9}Be(d,n)^{10}B were simulated using each code. Due to the limited number of experimental data points available for the ^{13}C(d,n)^{14}N (enriched ^{13}C target) and the lack of information on the degree of enrichment used in these studies, carbon in natural abundance (^{nat}C) was used for simulations of this reaction.

The minimum and maximum incident ion energies (E_i) simulated for each reaction have been summarised in Table 5. Each simulation uses a mono-energetic beam with a single discrete incident ion energy E_i per run. Multiple runs at different E_i values across these ranges were performed. These energy windows were chosen based on the reaction threshold energy (E_t), the energies over which experimental reference data were available and which incident ion energies are used in practice for current BNCT facilities. To determine an appropriate number of primary particles to use in the simula-

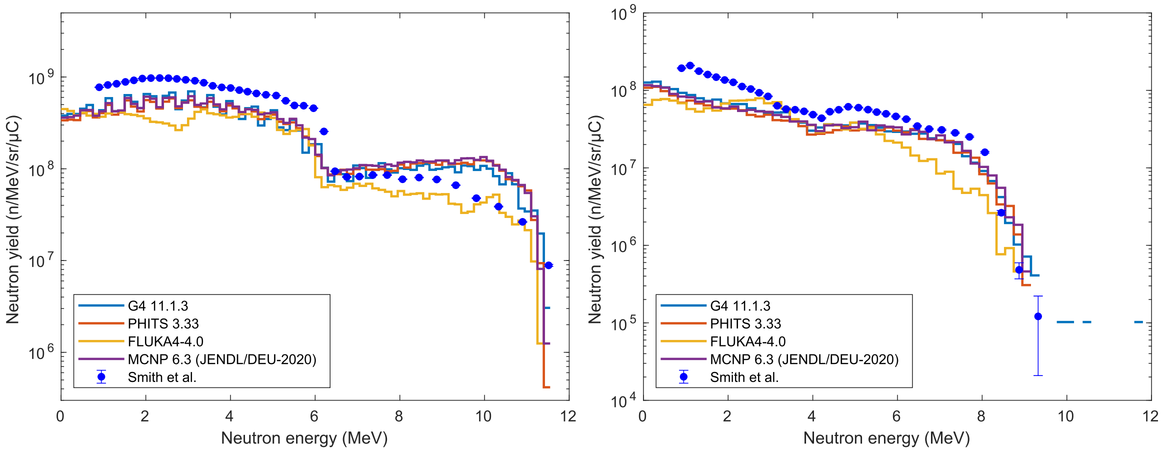

(a) $\theta = 0°$ (b) $\theta = 120°$

Fig. 9. Neutron energy spectra for ^{9}Be(d,n)^{10}B reaction with incident deuteron energy 7 MeV in (a) the forward direction ($\theta = 0°$) and (b) the backwards direction ($\theta = 120°$) with respect to beam direction. Results from each code compared to reference data from Smith et al. [76]. MCNP uses the JENDL/DEU-2020 cross section data.

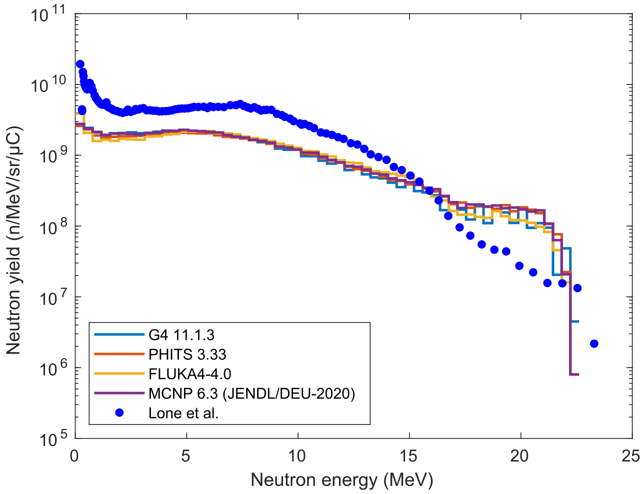

Fig. 10. Neutron energy spectra for the ^{9}Be(d,n)^{10}B reaction with incident deuteron energy of 18 MeV at in the forward direction ($\theta = 0°$) with respect to beam path. Results from each code are compared to reference data from Lone et al. [57]. MCNP uses the JENDL/DEU-2020 cross section data.

Table 5
Incident ion energy (E_i) range chosen for each simulated reaction. Units of energy are presented in MeV.

Reaction	E_{min}	E_{max}
^{7}Li(p,n)^{7}Be	1.89	10
^{9}Be(p,n)^{9}B	2.2	30
^{9}Be(d,n)^{10}B	1.25	20
C(d,n)N	0.75	20

tions, test simulations were performed using a representative scenario in which the number of simulated particles for each energy E_i is increased until the ratio of the inter-run standard deviation to the mean ($\sigma/\bar{x}$) for the total neutron yield ($n/\mu C$) declines below an arbitrary threshold of 5%. The number of primary particles used for each simulation condition is provided in the Supplementary Materials S1.3.

3.2. Data processing and analysis

The raw output from each simulation consists of a list of all particles (including neutrons) that have crossed the scoring sphere boundary surrounding the neutron production target, with corresponding information including particle type, kinetic energy (MeV), and position on the sphere. A 0 mm (effectively 0 eV) production cut was applied in each code where possible so secondary generation is tracked down to transport thresholds, meaning that particles recorded may originate either from the primary ion-target interaction or from the subsequent in-target cascade. This approach mirrors experimental practice where all neutrons escaping the target are registered, regardless of the origin of their generation within the cascade. This output is processed to derive total neutron yield (n/μC), angular neutron yield (n/sr/μC) and energy spectra (n/MeV/sr/μC).

To obtain neutron production yield (n/μC), the number of neutrons crossing the sphere's boundary (over the full 4π steradians of solid angle) is normalised by the charge of the incident ion beam (number of particles), measured in microcoulombs (μC), to account for variations in beam intensity (variation in the number of particles):

$$n/\mu C = \frac{N_n}{Q_{beam}} \tag{1}$$

where N_n is the number of neutrons crossing the scoring sphere boundary, and Q_{beam} is the total charge transferred by the incident beam in μC.

Angular neutron yield (n/sr/μC) is similarly calculated, but by counting the neutrons passing through the circular cap (analysis region in Fig. 2) corresponding to 1 steradian (sr)[5] centred at the angle of interest (θ), with the azimuth angle fixed at $\phi = 90°$ (YZ plane). The yield is calculated in increments of 5 degrees over the range of $\theta = 0°$ to $\theta = 180°$, assuming symmetry across all geometrically equivalent polar angles around the sphere. This step size was chosen as a balance between angular resolution, plot readability and data analysis efficiency.

Energy spectra are obtained by normalising the neutron yield (in the direction of interest) in each energy bin by the bin width in MeV and beam charge:

$$n/MeV/sr/\mu C = \frac{N_{n,sr}(\theta)}{\Delta E \times Q_{beam}} \tag{2}$$

where $N_{n,sr}$ is the number of neutrons per steradian emitted at the specified angle θ and ΔE is the energy bin width.

---

[5] Area (A) = r^2 where r is the radius of the sphere

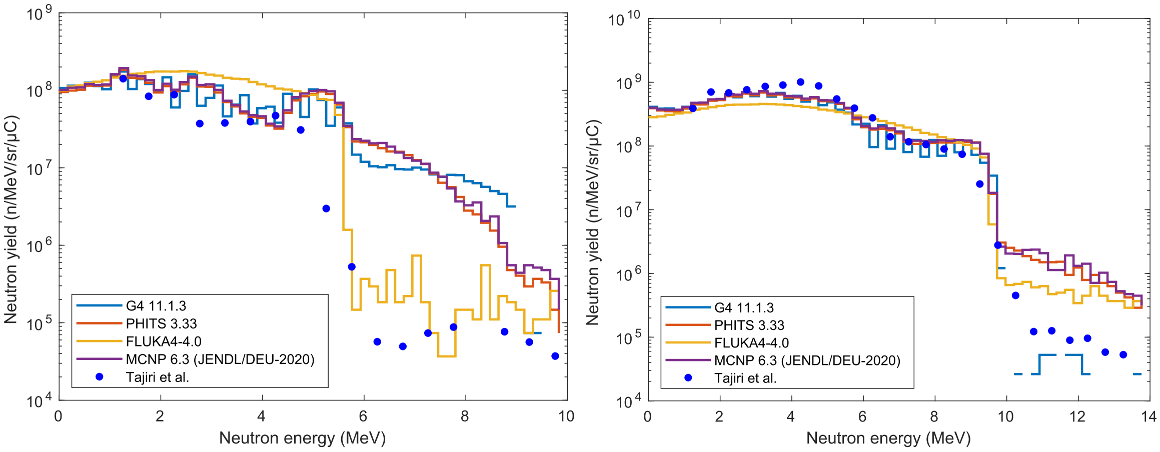

(a) 6 MeV (b) 10 MeV

Fig. 11. Neutron energy spectra for the C(d,n)N reaction for intermediate incident deuteron energies compared to reference data from Tajiri et al. [66] at 0° relative to beam direction at (a) 6 MeV and (b) 10 MeV compared to reference data at 5 MeV and 9 MeV, respectively.

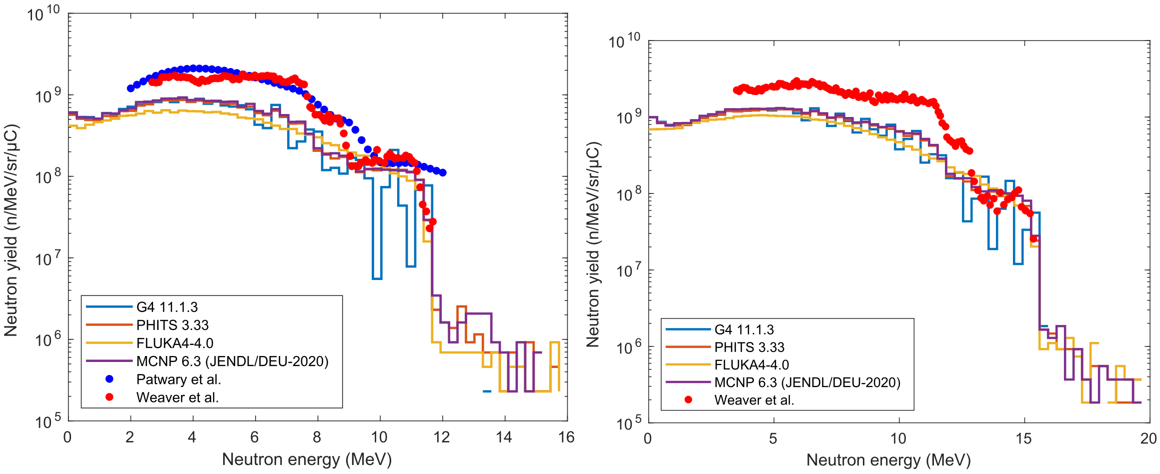

(a) 12 MeV (b) 16 MeV

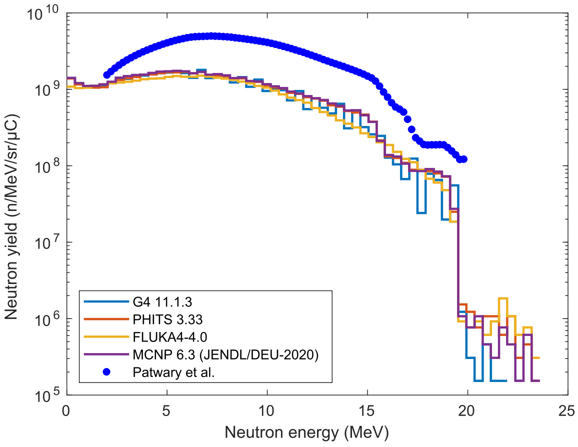

(c) 20 MeV

Fig. 12. Neutron energy spectra for the C(d,n)N reaction with incident deuteron energy of (a) 12 MeV, (b) 16 MeV and (c) 20 MeV in the forward direction ($\theta = 0°$ with respect to beam direction). Results from each code is compared to reference data from Patwary et al. [68] and Weaver et al. [65]. Data from Weaver et al. is slightly offset from the forward direction at 3.5°. MCNP uses the JENDL/DEU-2020 cross section data.

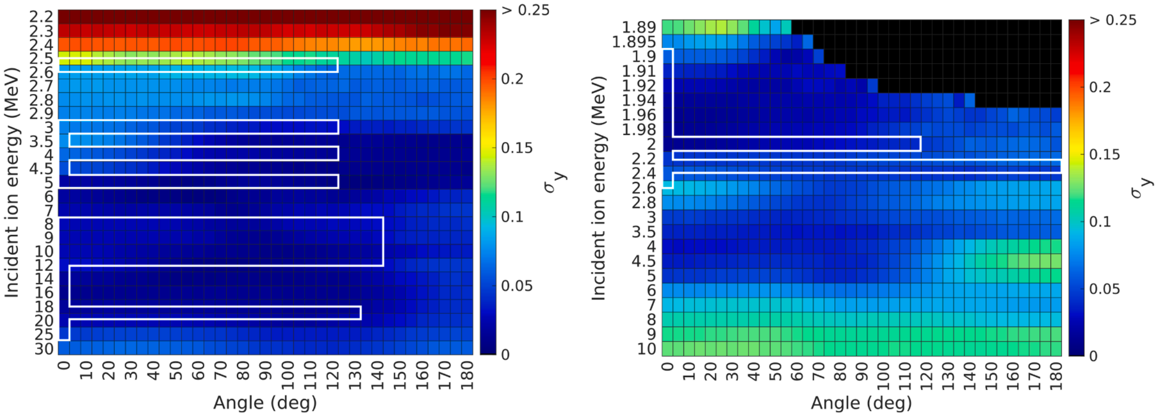

(a) ^{9}Be(p,n)^{9}B (b) ^{7}Li(p,n)^{7}Be

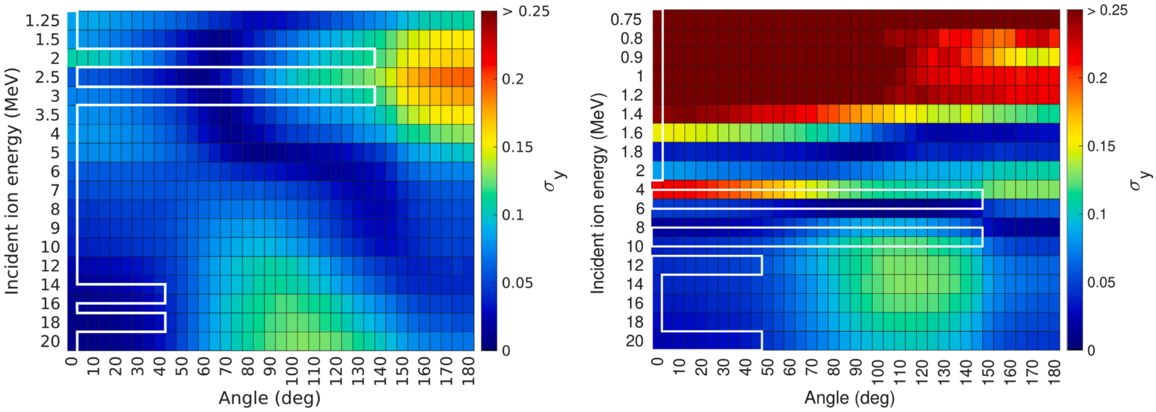

(c) ^{9}Be(d,n)^{10}B (d) C(d,n)N

Fig. 13. The standard deviation of the log transformed yield (σ_y) simulated across all MC codes for the (a) ^{9}Be(p,n)^{9}B, (b) ^{7}Li(p,n)^{7}Be, (c) ^{9}Be(d,n)^{10}B, and (d) C(d,n)N reactions. This is presented for the chosen incident proton energies simulated at angles from 0° to 180°. Regions surrounded by white borders indicate energy-angle combinations that have associated experimental datasets.

All error bars in the figures for the simulation results in this paper represent confidence intervals of ±2 standard errors of the mean (SEM).

3.3. Comparison metrics

The total neutron yield and the yield within the angular range from 0° (forward direction) to 180° (backward direction) are calculated for each simulation. To quantitatively compare the simulated neutron production yield of each reaction (both total yield and yield in the forward direction) against available experimental reference data, the ratio $r = \frac{S_i}{R_i}$ is calculated, where S_i is the simulation result and R_i is the corresponding reference data at incident ion energy i. For energies not directly simulated, linear interpolation was used.

Complementing these individual comparisons, the Mean Relative Error (MRE) was calculated for each simulation code to provide an aggregated measure of the deviation between simulated and reference yields across the entire incident energy range:

$$MRE = \frac{1}{N}\left[\sum_{i=1}^{N}\frac{|S_i - R_i|}{R_i}\right] \tag{3}$$

where N is the number of data points, S_i is the simulated value, and R_i is the experimental value. When multiple reference datasets were available, we calculated the average MRE ($\overline{MRE}$) to evaluate the overall agreement between simulation and experiment over the energy range.

To address the presence of large differences in scale between datasets, and significant differences in magnitude within single datasets, the symmetric Mean Absolute Percentage Error (sMAPE) has been chosen for comparing the performance of simulation against reference data for neutron energy spectra:

$$\text{sMAPE} = \frac{1}{N}\sum_{i=1}^{N}\frac{|S_i - R_i|}{\left(|S_i| + |R_i|\right)/2}$$

The value of sMAPE is bound between $0 < \text{sMAPE} < 2$, with 0 indicating perfect agreement, and 2 representing maximum possible disagreement, occurring when one value is non-zero and the other is zero.

To quantify the overall agreement of each code output with the shape of available experimental data points for angular distribution and neutron spectra across various reaction and incident ion energy combinations, the Pearson Correlation Coefficient (PCC) has been calculated:

$$PCC = \frac{\sum_{i=1}^{n}(S_i - \overline{S})(R_i - \overline{R})}{\sqrt{\sum_{i=1}^{n}(S_i - \overline{S})^2\,\sum_{i=1}^{n}(R_i - \overline{R})^2}} \tag{4}$$

where $\overline{S}$ and $\overline{R}$ are the mean values of the simulation and experimental yields (data points), respectively. The value of PCC is bound between $-1 < \text{PCC} < 1$, with 1 indicating perfect shape agreement and -1 indicating a perfect inverse correlation.

To benchmark the simulated neutron yield of the MC codes against one another and assess the variability between the codes for each reaction, the standard deviation of the log-transformed yields (σ_y) has been calculated:

$$\sigma_y = \sqrt{\frac{\sum_{i=1}^{N}(log_{10}(x_i) - \overline{x})^2}{N-1}} \tag{5}$$

where N is the number of different simulation codes evaluated, x_i is the neutron yield, and $\overline{x}$ is the mean of the log-transformed yield. This metric highlights where the consistencies and discrepancies between the codes lie for each reaction due to the differences in cross-section data libraries, models and the fundamental workings of each code, providing a measure of consensus between the codes. σ_y is plotted as a two-dimensional heatmap function of energy and scoring surface angle with respect to the target; energies and angles for which there is a larger disagreement between the models will be highlighted as 'hot' regions of this map.

3.4. Computational performance

To evaluate the relative computational performance of each Monte Carlo code in the context of simulating low-energy neutron production target reactions, the single-core throughput (defined as the mean of the number of primary particles processed per second across multiple runs) was measured for equivalent simulations of each reaction implemented in each Monte Carlo code.

A set of E_i energies across the energy range of each reaction have been chosen for comparison. 5 runs were completed for each E_i simulated. Simulations using each Monte Carlo code have been performed used the standard (developer-recommended) library linking compilation, with Geant4 and MCNP using dynamic libraries, while PHITS and FLUKA use static libraries. PHITS was compiled using the GFortran compiler rather than the Intel Fortran compiler. Default particle cuts were used for all codes, and step limits were not implemented for these tests. All simulations were performed using Intel Xeon E5-2650 v3 CPUs 2.30GHz. Each run was performed using a single core (single thread). To minimise competition effects on computational throughput results between simulations on the same compute node, no more than 15 cores (single-threaded runs) were in use at one time (on a 40-core node). The simulation initialisation time was subtracted from the reported run time for calculating computational performance (particles/s). In cases (PHITS, MCNP) where initialisation time was not mentioned in the simulation output, the total CPU time taken to run all particles was used, and enough particles were run to ensure that any contribution of initialisation was negligible.

4. Results and discussion

4.1. Neutron yield

To provide a comprehensive evaluation of the performance of all codes in predicting experimental neutron yield for each reaction, the total neutron yield and yield in the forward direction ($\theta = 0°$) have been compared to experimental datasets across the chosen incident ion energy range. For clarity, a summary of the best overall codes determined via the lowest $\overline{\text{MRE}}$ value between simulation and reference data is presented in Table 6. The full set of MRE results for neutron yield is provided in Supplementary Materials Section S2.5.

The yields for the ^{9}Be(p,n)^{9}B reaction simulated by each Monte Carlo code are presented in Fig. 3. All codes predict very similar total neutron yields (Fig. 3a) for E_i energies of 5–14 MeV, with larger discrepancies emerging at energies above and below this band. At E_i = 2.3 MeV, PHITS and FLUKA predict ∼40% lower yield than Geant4 and MCNP. Experimental reference data from Hawkesworth [50], Stephens and Miller [51] and Atta and Scott [52] are included for comparison. While the data from Hawkesworth [50] and Stephens and Miller [51] are provided as regression lines with no explicit data points, the predictions of all codes are in the same order of magnitude to these fits with Geant4 and MCNP providing the closest result to Hawkesworth et al. at low energies (see inset, Fig. 3a). Geant4, MCNP and PHITS show close agreement relative to experimental data from Atta and Scott [52], while FLUKA predicts lower yields within this range. Based on the average MRE values (Table 6), Geant4, MCNP and PHITS achieve the best overall performance for total neutron yield.

For simulated yield in the forward direction (Fig. 3b, $\theta = 0°$), all codes predict similar yields for proton energies between 5–30 MeV, with some divergence between codes emerging below 5 MeV. No experimental data is currently available below 3 MeV. For E_i in the range of 9–12 MeV, all codes are in close agreement with data presented by Lychagin et al. [53]. PHITS provides the closest agreement with Yue et al. [54] and Howard et al. [55] for energies in the range 3–5 MeV. Simulated neutron yields from all codes at higher incident energies lie between the results presented by Brede et al. [56] and Lone et al. [57]. Overall, the four codes exhibit statistically comparable performance across all datasets for yield in the forward direction of the ^{9}Be(p,n)^{9}B reaction (Table 6).

The simulated total neutron yield and yield in the forward direction for the ^{7}Li(p,n)^{7}Be reaction by each code are shown in Fig. 4. For total neutron yield (Fig. 4a), experimental data is available for this reaction across almost the entire energy range, with the most recent measurements published by Martín-Hernández et al. [58] in 2019. At higher incident ion energies, FLUKA provides the best agreement with Atta and Scott [52] and Scott [59]. At lower incident energies, PHITS shows the best agreement with Lee and Zhou [60] and Martín-Hernández et al. [58]. For simulated yield in the forward direction (Fig. 4b), available reference data is present only up to $E_i = 2.5$ MeV. This presents a gap in the literature and highlights the need for experimental reference data for energies up to 10 MeV. Across the full energy range, FLUKA and PHITS achieve the lowest comparable average MRE values for total neutron yield while for forward directed yield up to 2.5 MeV gives comparable MRE values for all codes (Table 6).

For the ^{9}Be(d,n)^{10}B reaction, experimental benchmarks for total neutron yield (Fig. 5a) are also limited. Similarly to the ^{9}Be(p,n)^{9}B reaction, both Hawkesworth [50] and Stephens and Miller [51] present regression lines with no explicit data points. Additional data points are provided by Kononov et al. [61] and Zuo et al. [63], who present yield measurements within the energy range of 0.95 MeV to 3 MeV. In this energy range, FLUKA provides the best agreement with experiment. The lack of data points above 3 MeV highlights the need for new total yield data up to 20 MeV. In contrast, experimental data points are available across the entire incident energy range from 1.25 to 20 MeV for neutron yield at 0° (Fig. 5b). All codes predict similar yields, with the exception of FLUKA. A large discrepancy between the codes and experimental data arises at higher E_i, with simulation data diverging from reference data by Meadows et al. [64] and Weaver et al. [65] up to 20 MeV. For both total yield and forward directed yield, Geant4, MCNP and PHITS achieve the lowest average MRE values across all experimental datasets (Table 6).

Simulation output for the C(d,n)N reaction is presented in Fig. 6. As in previous cases, FLUKA's predicted yield is inconsistent with the predictions of the other codes for this reaction. The number of available experimental data points is limited, both for total neutron yield and yield in the forward direction. For total neutron yield (Fig. 6a) most data points lie at lower incident energies ($E_i < 3$ MeV) , with Tajiri et al. [66] providing two data points at 5 MeV and 9 MeV. Across these experimental datasets, all codes achieve comparable performance using the average MRE metric. For neutron yield in the forward direction (Fig. 6b), more data is available at higher E_i, with a notable gap in the literature for energies between ∼2 MeV and 9 MeV. Using these points as a benchmark, Geant4, MCNP and PHITS provide the best agreement with the available experimental datasets

Given the available reference experimental data used to compare the simulation output for each of the proposed reactions, a summary of the overall best performing code/s for the simulation of total neutron yield and yield at 0° is presented in Table 6. This can be used to help inform the choice of Monte Carlo code for simulating the neutron yield of these reactions. It is important to note that in a few cases (denoted by *), there is a lack of available experimental data points across the entire incident energy range, and thus future work in measuring TTY for these reactions is needed.

Table 6
A summary of the overall best performing code/s for the simulation of the total neutron yield and yield at 0° for each reaction. This is determined by taking the lowest average MRE ($\overline{\text{MRE}}$) value between simulation and available reference data. Values that are statistically indistinguishable from the lowest $\overline{\text{MRE}}$ are also included. Uncertainties for $\overline{\text{MRE}}$ represent the standard error of the mean. * denotes that there is a lack of available data points across the incident energy range for comparison with the MC codes in the respective cell.

	Total yield		Yield at 0°	
	Code	$\overline{\text{MRE}}$	Code	$\overline{\text{MRE}}$
^{9}Be(p,n)^{9}B	G4 11.1.3 PHITS MCNP	0.17 ± 0.03* 0.20 ± 0.06 0.16 ± 0.04	G4 11.1.3 PHITS FLUKA MCNP	0.34 ± 0.19 0.22 ± 0.16 0.37 ± 0.15 0.37 ± 0.22
^{7}Li(p,n)^{7}Be	PHITS FLUKA	0.12 ± 0.04 0.09 ± 0.03	G4 11.1.3 PHITS FLUKA MCNP	0.44 ± 0.13* 0.48 ± 0.12 0.56 ± 0.21 0.45 ± 0.14
^{9}Be(d,n)^{10}B	G4 11.1.3 PHITS MCNP	0.15 ± 0.02* 0.18 ± 0.03 0.16 ± 0.03	G4 11.1.3 PHITS MCNP	0.29 ± 0.15 0.29 ± 0.17 0.28 ± 0.07
C(d,n)N	G4 11.1.3 PHITS FLUKA MCNP	1.21 ± 0.64* 0.71 ± 0.24 0.72 ± 0.09 1.33 ± 0.72	G4 11.1.3 PHITS MCNP	0.33 ± 0.09* 0.33 ± 0.08 0.31 ± 0.08

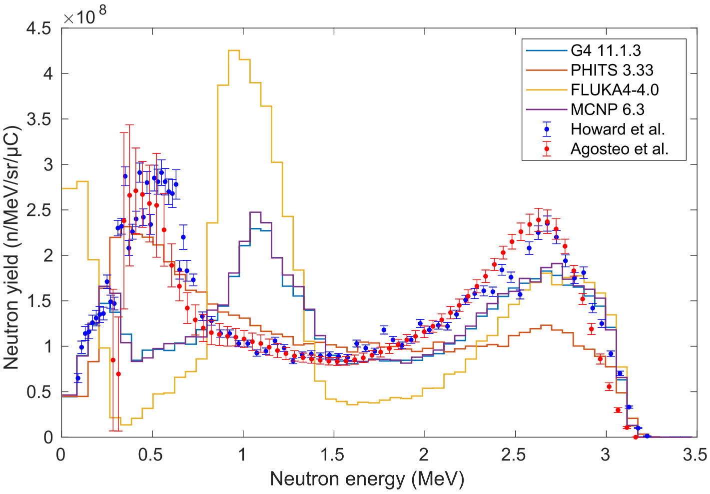

Fig. 14. Neutron energy spectra for the ^{9}Be(p,n)^{9}B reaction with incident proton energy of 5 MeV in the forward direction ($\theta = 0°$). Codes are compared to reference data obtained from Howard et al. [55] and Agosteo et al. [70].

4.2. Angular distribution

The complete simulated angular distributions across all codes for each reaction and the chosen energies can be found in Supplementary Materials Sections S2.7–S2.10. In the main text we present benchmarking comparisons only for the ^{9}Be(p,n)^{9}B and C(d,n)N reactions where experimental data is available. For all reactions at the energies simulated, neutron emission is highest in the forward direction. This characteristic is most prominent at higher incident particle energies.

^{9}Be(p,n)^{9}B neutron yields from 0 to 180 degrees at E_i of 8 MeV, 9 MeV and 10 MeV are presented in Fig. 7 together with reference data from Lychagin et al. [53] with E_i of 8.26 MeV, 9.18 MeV and 10.24 MeV, respectively. When compared to these measurements, most codes predict angular distributions well at angles up to 140°, particularly in the forward direction ($\theta < 90$). FLUKA tends to underestimate neutron yield at all angles - especially so closer to the 0° and 180° directions. This underestimation is smallest between about 30° and 75°. Beyond 90° and especially past 140°, all codes begin to diverge from one another. The plots in Supplementary Material Section S2.7.1 further illustrate these differences, with PHITS and FLUKA consistently generating angular distributions different to those obtained from Geant4 and MCNP, particularly at lower energies.

Fig. 8 compares the angular distribution of the C(d,n)N reaction at 12 MeV and 20 MeV to results reported by Patwary et al. [68]. At both incident E_i energies, significant discrepancies are observed between the experimental and simulated angular distributions output by each code from 0° to 45°. At 0°, simulated yield is ~40% lower than the measured values for both 12 MeV and 20 MeV. In both cases, the yield presented by FLUKA is lower compared to the other codes. This underestimation may be due to limitations in the nuclear reaction models or cross-section data used by the MC codes for C(d,n)N reactions, however, additional independent measurements are needed to confirm whether these discrepancies arise from code limitations or experimental error, particularly in the forward direction.

4.3. Neutron spectra

The neutron energy spectrum is another major consideration for the design of the BSA system. The energy distribution of the neutrons emitted from the neutron production target inform the design of both the moderator and shielding/filtering needed to achieve the desired neutron spectra for the neutron source application. The simulated energy spectra from each code for all reactions can be found in Supplementary Material Sections S2.7–S2.10. A summary of the Pearson Correlation Coefficient (PCC), which captures shape agreement independent of absolute yield, and Symmetrical Mean Absolute Percentage Error (sMAPE) values calculated for the energy spectra presented in this section is shown in Table 7.

The precision of the total neutron spectra generated by each code is evaluated for the ^{9}Be(p,n)^{9}B reaction using a combination of experimental measurements from Howard et al. [55], Agosteo et al. [70] and Lychagin et al. [53]. Fig. 14 shows the neutron spectra for this reaction with $E_i = 5$ MeV at 0°. Results obtained with PHITS, which uses the JENDL-5 data library, provide the best overall agreement with the experimental data from Howard et al. [55] and Agosteo et al. [70], displaying the lowest sMAPE values of 0.28 ± 0.20 and 0.32 ± 0.32 respectively, and highest PCC values. The results obtained with both Geant4/MCNP (ENDF) and FLUKA (PEANUT model) are inconsistent with the shape of the measured spectra, exhibiting a notable broad peak at ~1 MeV which is absent in the experimental data. Although PHITS provides the best overall match with the experimental spectra, there is still a severe underestimation (of around 50%) at higher energies for $E_i = 5$ MeV as well as a less pronounced underestimation at lower neutron energies.

At $E_i = 4$ MeV, similar discrepancies in the lower energy range can be seen for both the forward and backward directions, as shown in Fig. 15. In the forward direction ($\theta = 0°$), PHITS provides the best agreement (PCC = 0.87) over all incident energies measured by Howard et al. [55]; however, the code overestimates the yield in the backwards direction ($\theta = 140°$), particularly at low energies. Further discussion on how JENDL-5 (using PHITS) performs against other data libraries and its predecessor JENDL-4.0/HE can be found in the paper by Kunieda et al. [71].

A comparison for a higher E_i energy at 9 MeV is shown in Fig. 16 against experimental data from Lychagin et al. [53] for 9.18 MeV. Results are similar in the forward direction ($\theta = 0$), with PHITS providing the most accurate estimation of the neutron spectral shape (PCC = 0.93). PHITS again underestimates neutron yield at lower neutron energies. For the backwards direction ($\theta = 140$), all codes produce spectra with lower sMAPE values between simulation and experimental results compared to those at 0°, however, there is still a large standard de-

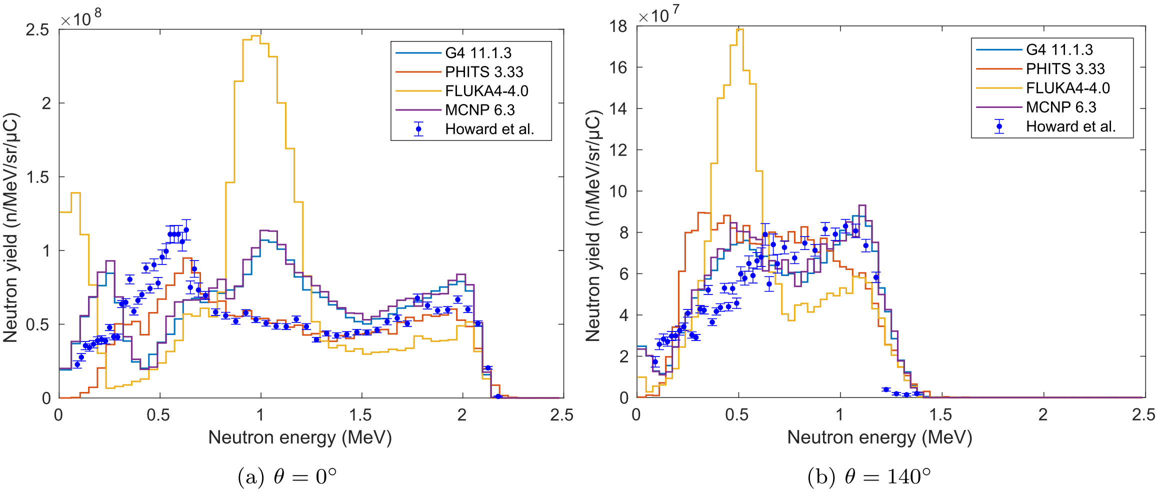

(a) $\theta = 0°$ (b) $\theta = 140°$

Fig. 15. Neutron energy spectra for the ^{9}Be(p,n)^{9}B reaction with incident proton energy of 4 MeV in the forward direction ($\theta = 0°$) and backwards direction ($\theta = 140°$) with respect to the beam path. Results from each code are compared to reference data from Howard et al. [55].

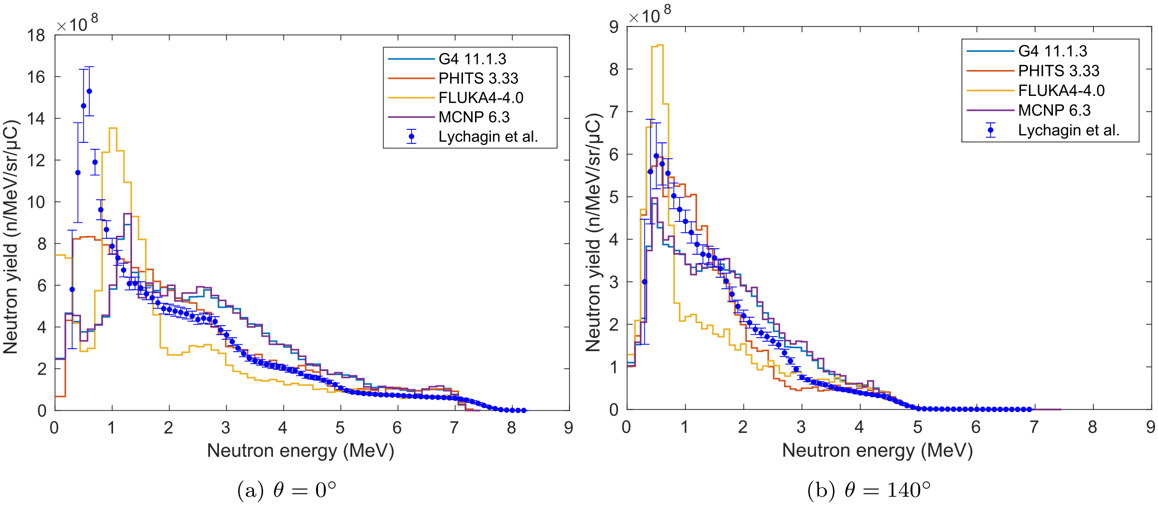

(a) $\theta = 0°$ (b) $\theta = 140°$

Fig. 16. Neutron energy spectra for the ^{9}Be(p,n)^{9}B reaction with incident proton energy of 9 MeV in the forward direction ($\theta = 0°$) and backwards direction ($\theta = 140°$) with respect to the beam path. Results from each code are compared to reference data from Lychagin et al. [53] ($E = 9.18$ MeV).

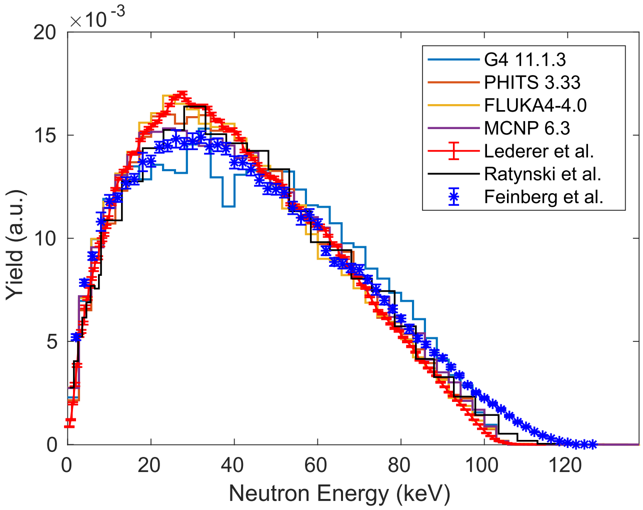

Fig. 17. Energy spectra of the ^{7}Li(p,n)^{7}Be reaction with an incident proton energy of 1.91 MeV simulated by each code against reference data from Lederer et al. [73], Ratynski and Käppeler [72] and Feinberg et al. [74]. Neutron yield has been normalised to unit area and is presented in arbitrary units (a.u).

viation (spread) in these values with each code both under and overestimating yields in different E_n ranges.

PHITS provides the overall most accurate reproduction of experimental neutron spectra across the energies available in the literature for the ^{9}Be(p,n)^{9}B reaction. Published experimental data for higher incident energies (> 9 MeV) is not currently available to our knowledge, but would be very useful for future work to validate each code for the simulation of this reaction.

For the ^{7}Li(p,n)^{7}Be reaction, experimental neutron energy spectra (angle-integrated) for incident proton energy of 1.91 MeV are available from Ratynski and Käppeler [72], Lederer et al. [73], and Feinberg et al. [74]. This data is shown in Fig. 17 against simulated total energy spectra (4π) at $E_i = 1.91$ MeV from each code. Feinberg et al. [74] and Ratynski and Käppeler [72] report spectra from E = 1.912 MeV. All data has been normalised to unit area. As shown in this figure, all codes are in good agreement with the energy spectra reported in literature. Geant4 slightly underestimates the yield at the 30 keV peak compared to the other codes.

The performance of each code relative to available reference data for the ^{9}Be(d,n)^{10}B reaction at low E_i (1.5 MeV) is shown in Fig. 18. The simulation results produce spectra with many features which are consistent with experimental data from both Guzek et al. [75] and Colonna et al. [67], including the spectral minima at ~1.2 MeV, ~2.6 MeV and

Table 7

A summary of the Pearson correlation coefficient (PCC) and Symmetrical Mean Absolute Percentage Error (sMAPE) values calculated for the energy spectra shown in this paper. Uncertainties presented for sMAPE values represent the standard deviation relative to the mean (SD).

Figure	Target reaction	Energy (MeV), Angle (°)	Code	PCC		sMAPE ± SD	
14	^{9}Be(p,n)^{9}B	5, 0		Howard	Agosteo	Howard	Agosteo
			G4 11.1.3	0.11	0.26	0.43 ± 0.39	0.40 ± 0.33
			PHITS	0.79	0.60	0.28 ± 0.20	0.32 ± 0.32
			FLUKA	−0.25	−0.05	0.86 ± 0.53	0.78 ± 0.44
			MCNP	0.08	0.23	0.44 ± 0.42	0.40 ± 0.34
15a	^{9}Be(p,n)^{9}B	4, 0		0°	140°	0°	140°
15b	^{9}Be(p,n)^{9}B	4, 140	G4 11.1.3	−0.08	0.82	0.52 ± 0.33	0.33 ± 0.39
			PHITS	0.87	0.61	0.28 ± 0.37	0.50 ± 0.42
			FLUKA	−0.11	0.34	0.83 ± 0.48	0.68 ± 0.40
			MCNP	−0.07	0.79	0.53 ± 0.34	0.36 ± 0.40
16a	^{9}Be(p,n)^{9}B	9, 0		0°	140°	0°	140°
16b	^{9}Be(p,n)^{9}B	9, 140	G4 11.1.3	0.69	0.96	0.59 ± 0.61	0.67 ± 0.71
			PHITS	0.93	0.98	0.43 ± 0.63	0.68 ± 0.77
			FLUKA	0.69	0.85	0.59 ± 0.62	0.78 ± 0.71
			MCNP	0.69	0.96	0.60 ± 0.61	0.76 ± 0.78
18	^{9}Be(d,n)^{10}B	1.5, 0		Guzek		Guzek	
			G4 11.1.3	0.75		0.63 ± 0.40	
			PHITS	0.80		0.63 ± 0.49	
			FLUKA	0.48		0.61 ± 0.51	
			MCNP	0.80		0.59 ± 0.45	
9a	^{9}Be(d,n)^{10}B	7, 0		0°	120°	0°	120°
9b	^{9}Be(d,n)^{10}B	7, 120	G4 11.1.3	0.96	0.96	0.51 ± 0.30	0.49 ± 0.18
			PHITS	0.97	0.96	0.58 ± 0.31	0.62 ± 0.31
			FLUKA	0.93	0.78	0.67 ± 0.36	0.73 ± 0.42
			MCNP	0.97	0.95	0.56 ± 0.29	0.56 ± 0.32
10	^{9}Be(d,n)^{10}B	18, 0	G4 11.1.3	0.79		0.85 ± 0.28	
			PHITS	0.80		0.89 ± 0.30	
			FLUKA	0.82		0.86 ± 0.33	
			MCNP	0.79		0.85 ± 0.30	
11a	C(d,n)N	6, 0		6 MeV	10 MeV	6 MeV	10 MeV
11b	C(d,n)N	10, 0	G4 11.1.3	0.93	0.96	1.23 ± 0.73	0.69 ± 0.61
			PHITS	0.85	0.97	1.16 ± 0.73	0.71 ± 0.64
			FLUKA	0.82	0.93	0.90 ± 0.46	0.68 ± 0.46
			MCNP	0.85	0.96	1.23 ± 0.73	0.72 ± 0.66
12a	C(d,n)N	12, 0		Patwary	Weaver	Patwary	Weaver
			G4 11.1.3	0.95	0.88	0.62 ± 0.15	0.56 ± 0.24
			PHITS	0.98	0.94	0.55 ± 0.18	0.46 ± 0.18
			FLUKA	0.97	0.93	0.59 ± 0.20	0.53 ± 0.19
			MCNP	0.98	0.94	0.54 ± 0.17	0.45 ± 0.17
12b	C(d,n)N	16, 0		16 MeV	20 MeV	16 MeV	20 MeV
12b	C(d,n)N	20, 0	G4 11.1.3	0.93	0.88	0.82 ± 0.30	1.08 ± 0.28
			PHITS	0.96	0.91	0.72 ± 0.28	1.02 ± 0.26
			FLUKA	0.93	0.89	0.84 ± 0.32	1.11 ± 0.28
			MCNP	0.96	0.90	0.67 ± 0.26	1.00 ± 0.28

~4 MeV corresponding to the maximum neutron energies associated with the residual ^{10}B nucleus. According to Colonna et al., the flat energy distribution seen in experimental spectra at energies above 1 MeV is the result of limited detector energy resolution which prevents higher-energy peaks and minima from being resolved. All codes provide good agreement with the only resolvable peak in this dataset (at 0.5 MeV). In comparison with the spectra published by Guzek et al., simulations using PHITS, Geant4 and MCNP reproduce the shape of the experimental energy distribution well (PCC = 0.75, 0.80, 0.80 respectively), including the magnitudes of the peaks at approximately 0.5 MeV, 1.6 MeV, and 3.5 MeV. The simulations tend to predict deeper minima at ~1.2 MeV, 2.6 MeV and 4.1 MeV compared to reported experimental data, however this is likely to be a result of limited spectral resolution of the experimental measurements. In the simulations, the minima also occur at a slightly higher energy compared to the experimental results (by 0.05-0.1 MeV). FLUKA provides the best estimate of neutron spectra between 1 MeV and 6 MeV, but does show large discrepancies with experimental values below 1 MeV.

Smith et al. [76] provide reference spectra for the ^{9}Be(d,n)^{10}B reaction at an intermediate E_i of 7 MeV. Fig. 9 shows the experimental spectra for this reaction at $\theta = 0°$ and at 120° together with the simulation spectra. The absolute yield reported by Smith et al. [76] is ~30% higher than the simulation data presented for both emission angles. When examining the relative shape of the neutron spectra at 0° (Fig. 9a), Geant4, PHITS and MCNP provide the best replication of neutron spectra relative to experiment below 6 MeV, with FLUKA showing discrepancies in yield and shape at ~2.6 MeV. However, above 6 MeV, FLUKA provides the best estimate of spectrum shape compared to the other codes, which all produce similar spectra. At 120° (Fig. 9b), all codes are in good agreement with the shape of the neutron spectra above ~6 MeV, with the exception of FLUKA which underestimates the yield. Below 4 MeV, Geant4, PHITS and MCNP display a similar spectral shape relative to the reference data, albeit with lower absolute yield in this energy range, while FLUKA diverges from experimental data at lower energies.

For the comparison of the spectra produced by each code at higher energies for the ^{9}Be(d,n)^{10}B reaction, Fig. 10 presents simulation results

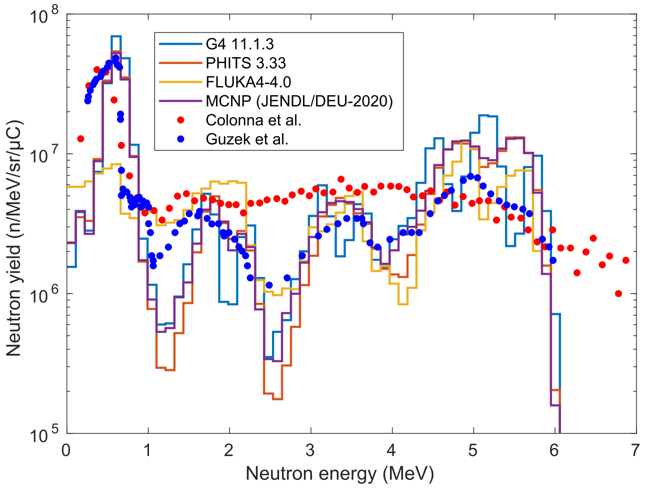

Fig. 18. Neutron energy spectra for the ^{9}Be(d,n)^{10}B reaction with incident deuteron energy of 1.5 MeV at 0° with respect to the beam direction. Results from each code are shown together with experimental reference data from Guzek et al. [75] and Colonna et al. [67]. The data by Guzek et al. has been renormalised by Capoulat et al. [15]. MCNP uses the JENDL/DEU-2020 cross section data.

for $E_i = 18$ MeV compared to experimental values from Lone et al. [57]. Similarly to Fig. 9, the experimental yield from Lone et al. [57] across the emission neutron spectra is ∼55% higher than simulation yield results. For the majority of the neutron energy range up to ∼15 MeV, simulation results from all codes replicate the shape of the spectra well. However, the maximum of the very broad peak at ∼7 MeV seen in the experimental data is shifted to ∼5 MeV in all simulation codes. Beyond 15 MeV, all codes overestimate the neutron yield relative to experimental data.

For the simulation of C(d,n)N energy spectra, reference data from Patwary et al. [68], Weaver et al. [65] and Tajiri et al. [66] is used to evaluate the simulation results. Intermediate incident deuteron energies of 6 MeV and 10 MeV are compared to 5 MeV and 9 MeV spectra respectively from Tajiri et al. [66] in Fig. 11. At $E_i = 6$ MeV (Fig. 11a), all codes are in good agreement with experimental spectra below ∼4.5 MeV, although FLUKA somewhat overestimates neutron yield between 2 MeV and 5 MeV. Above 5 MeV, FLUKA provides the best agreement of all codes relative to both the shape of the experimental spectra and error, supported by a sMAPE of 0.90 ± 0.46 and the lowest standard deviation relative to the other MC codes that greatly overestimate neutron yield. For $E_i = 10$ MeV (Fig. 11b), the accuracy of the shape of spectra for all MC codes improves (higher PCC) compared to lower incident particle energies, with all MC codes correctly predicting a drop in yield past 8 MeV as in experiment. However, MCNP, PHITS and FLUKA overestimate the relative yield, while Geant4 underestimates this yield.

Simulated C(d,n)N neutron spectra from higher incident deuteron energies of 12 MeV, 16 MeV and 20 MeV are presented in Fig. 12 and compared against experimental data from Patwary et al. [68], who provide data for 12 MeV and 20 MeV, and Weaver et al. [65], who provide data for 16 MeV and 20 MeV. In all cases, the reported experimental data indicates a higher yield than that predicted by the simulations. This results in high sMAPE values for all MC codes. At 12 MeV and 16 MeV, all MC codes match the shape of the experimental spectra quite well for both incident particle energies. Relative to the other MC codes, FLUKA consistently underestimates the neutron yield by the largest amount. It should also be noted that for $E_i = 12$ MeV, the spectral shape and yield from Patwary et al. [68] and Weaver et al. [65] are inconsistent between energies of 3 MeV and 6 MeV. For $E_i = 16$ MeV, the experimental neutron yield is comparable to resulting simulation data between 12 MeV and 15 MeV. At $E_i = 20$ MeV, the fit of simulation results to the spectral shape of the experimental data is worse than for 12 and 16 MeV (even accounting for the lower total yield), with a relative overestimation of yield at energies below 5 MeV (confirmed by lower PCC values compared to the lower incident energy spectra).

4.4. Inter-code discrepancies in neutron angular and spectroscopic yield

Sections 4.1–4.3 report the agreement between simulation outputs and experimental measurements for available datasets in literature. This section evaluates the consistency between the four Monte Carlo codes for each reaction, including in regions without experimental benchmarks. In these regions where no experimental data exist, simulation results should be considered predictive only.

To characterise the level of agreement across the codes, the inter-code standard deviation in total neutron yield from 0° to 180°, as well as spectroscopic neutron yield at 0°, is presented. This provides a comprehensive view of code performance over the full range of incident energies, and insight into how consistently the recommended physics models and data libraries are implemented across the codes. Where experimental benchmarks exist, close agreement between the codes indicate convergence towards physically accurate modelling, and comparison against this data allows code accuracy to be directly assessed. In contrast, where no benchmarks are available, the level of inter-code agreement serves as an indicator of predictive confidence: a large spread suggests divergent model behaviour and low confidence in individual predictions, whereas a small spread signals code consistency but still only offers provisional confidence until experimental measurements are available. Notable discrepancies may arise from a combination of factors including differences in models, cross-section data libraries (particularly where experimental measurements are scarce), near-threshold effects and variations in particle transport algorithms. However, because these factors often act in tandem with one another, and the source code of PHITS, FLUKA and MCNP is not publicly accessible, it is challenging to isolate the exact source of this disagreement.

Fig. 13 presents the standard deviation of the log-transformed yield (σ_y) at each evaluated energy-angle combination to illustrate the variability in angular neutron yield predictions between the codes for each reaction at the chosen incident energies. A visual indication of where experimental benchmarks exist has been overlaid. As these plots provide a high-level summary, a more detailed comparison of how each code performs against the others for each reaction is included in Supplementary Material Section S2.3.

The simulations of the ^{9}Be(p,n)^{9}B reaction (Fig. 13a) show that there are large variations between the codes for $E_i < 5$ MeV. For $E_i \geq 5$ MeV, all codes are highly consistent with one another for the simulation of this reaction ($\sigma_y < 0.05$). Both Geant4 and MCNP use similar data libraries; ENDF/B-VIII.0 and ENDF/B-VII.0 respectively. As such, they both produce very similar neutron yield results (see Supplementary Materials Section S2.3.1) across all emission angles, with a maximum difference of ∼15%. PHITS and FLUKA exhibit larger discrepancies at lower incident proton energies compared to Geant4 and MCNP.

All codes predict mutually consistent yields up to ∼3.5 MeV for the ^{7}Li(p,n)^{7}Be reaction. Beyond 3.5 MeV, variation between the codes increases, particularly in the backwards directions ($\sigma_y > 0.1$). At incident energies from threshold up to 1.94 MeV, all codes predict that neutrons are predominantly emitted in the forward direction, as demonstrated by the negligible yield (black pixels) resulting from all codes for the backwards directions in Fig. 13b. The cross-section libraries and models used by each code for the ^{7}Li(p,n)^{7}Be reaction are the same as those used for the ^{9}Be(p,n)^{9}B reaction. Unlike the ^{9}Be(p,n)^{9}B reaction, the yields predicted by Geant4 and MCNP for the ^{7}Li(p,n)^{7}Be reaction are quite different, despite the similar cross section data libraries used (see Supplementary Materials Section S2.3.2). From ∼2.2 MeV-3 MeV, Geant4 exhibits an inconsistent angular yield distribution compared to the other codes. Both MCNP and FLUKA display an increased yield compared to Geant4 and PHITS by approximately >30% at energies up to 10 MeV.

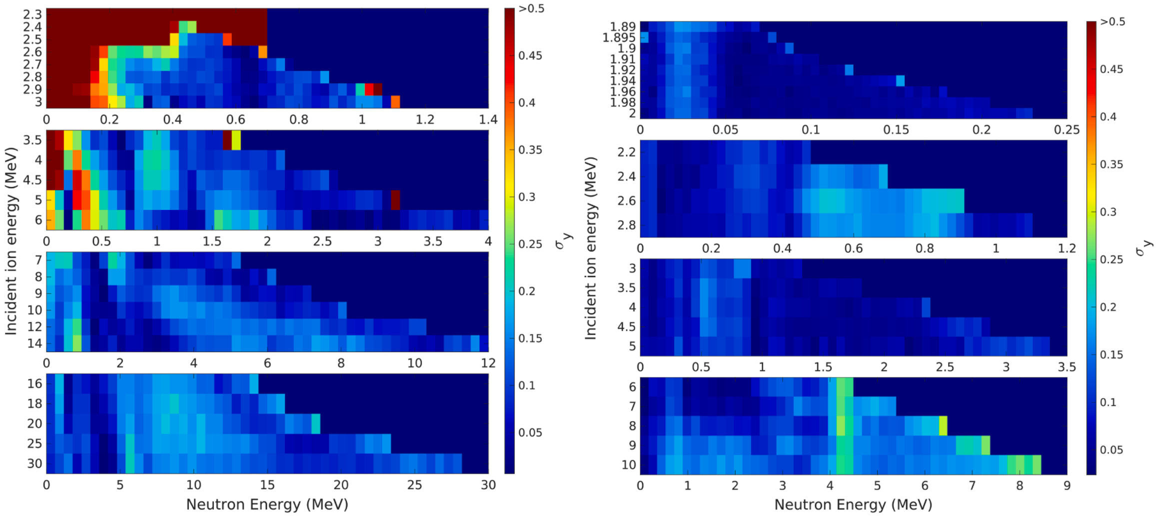

(a) ^{9}Be(p,n)^{9}B (b) ^{7}Li(p,n)^{7}Be

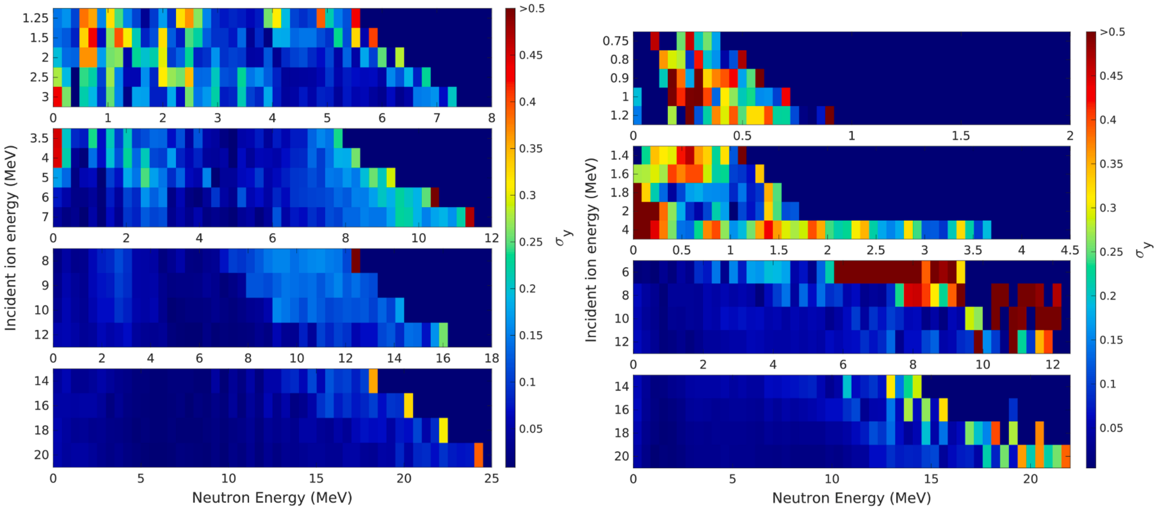

(c) ^{9}Be(d,n)^{10}B (d) C(d,n)N

Fig. 19. The standard deviation of the log transformed spectral yield (σ_y) at $\theta = 0°$ simulated across all MC codes for the (a) ^{9}Be(p,n)^{9}B, (b) ^{7}Li(p,n)^{7}Be, (c) ^{9}Be(d,n)^{10}B, and (d) C(d,n)N reactions. Note: Larger σ_y values at low incident ion energies may be skewed by the low absolute yields in these regions, which amplify statistical fluctuations and apparent code variability.

For the simulation of deuteron interactions with beryllium and carbon targets, both Geant4 QGSP_BIC_AllHP and PHITS utilise the JENDL/DEU-2020 data library for beryllium. FLUKA and MCNP rely on their own inbuilt models; however, as previously mentioned, the JENDL/DEU-2020 ACE files have been added to MCNP. As shown in Fig. 13c, simulations of the ^{9}Be(d,n)^{10}B reaction exhibit a high degree of variability across a wide range of energies. Through inspection of the specific differences between the yield predicted by different codes (Supplementary Materials Section S2.3.3), Geant4, MCNP and PHITS exhibit consistent neutron yields across all energies. The variability is principally due to discrepancies exhibited by the FLUKA code, with large differences in yield (>50%) at a majority of the energy-angle combinations compared to the other codes. This is likely attributable to FLUKA's use of internally modelled deuteron-induced reactions, in contrast to the evaluated cross-section libraries (e.g., TENDL, JENDL/DEU-2020) used by Geant4, MCNP, and PHITS. Similar consistencies and discrepancies between the codes are seen for the C(d,n)N reaction, with FLUKA introducing majority of the variability. However, larger variability between yield predicted by different codes ($\sigma_y > 0.25$) is present at the lower incident ion energies.

Fig. 19 presents the standard deviation of the log-transformed spectral yield (σ_y) in the forward direction ($\theta = 0°$) for a range of ion energies. It is important to note that the variation in σ_y at lower incident ion energies, or towards the tail end of each spectrum, is likely skewed by the lower neutron yields obtained in these regions, causing statistical fluctuations between the yields predicted by the different Monte Carlo codes to appear disproportionally large. For direct observation of the neutron spectra used to generate these plots, spectra for each incident ion energy can be found in Supplementary Material S2.7–S2.10.

Across all reactions, greater variability in predicted spectroscopic yield between the codes is evident at lower incident ion energies (E_i), with the exception of the ^{7}Li(p,n)^{7}Be reaction (Fig. 19b). This is likely due to a combination of factors that include cross-section differences between the codes, near-threshold effects, and differences in model implementations at lower energies. At higher E_i energies for proton induced reactions, σ_y remains elevated (up to ~0.2), particularly within E_n ranges of 5 MeV to 10 MeV for the ^{9}Be(p,n)^{9}B reaction (Fig. 19a) and 4 MeV to 5 MeV for the ^{7}Li(p,n)^{7}Be reaction. For E_i of 2.2 MeV to 2.8 MeV for the ^{7}Li(p,n)^{7}Be reaction, there is also a high σ_y of ~0.22 within the E_n range of 0.4 MeV to 0.9 MeV. Upon analysis of the spectra

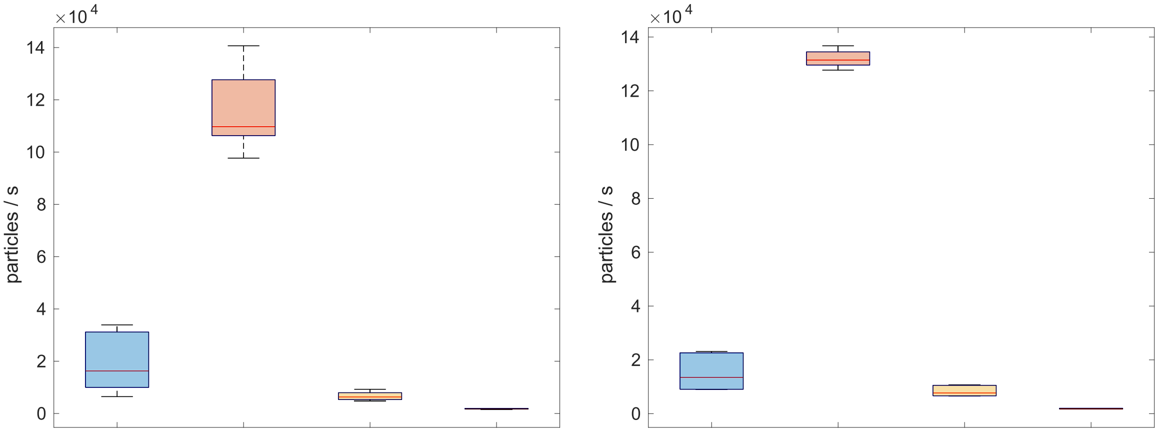

(a) ^{9}Be(p,n)^{9}B (b) ^{7}Li(p,n)^{7}Be

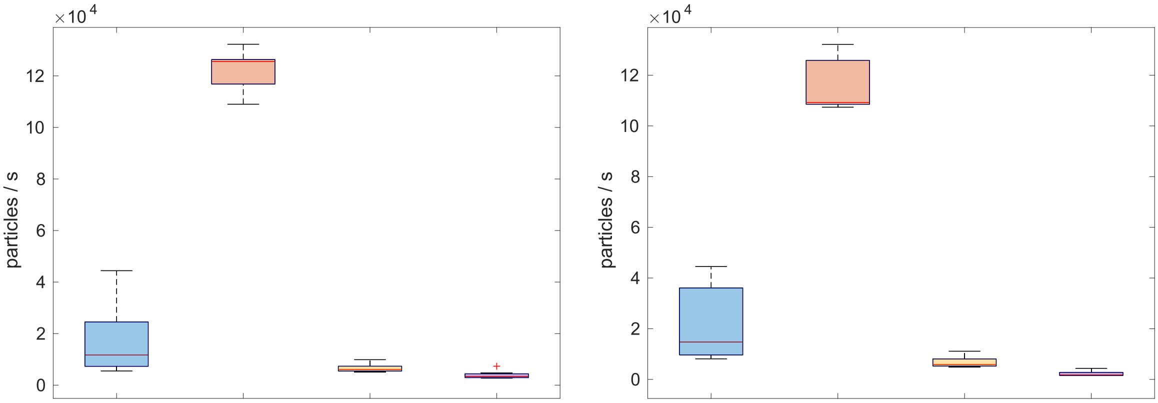

(c) ^{9}Be(d,n)^{10}B (d) C(d,n)N

Fig. 20. Single-threaded computational throughput measured in particles per second for each code across all simulated reactions.

within S2.8.2, this is due to a decrease in yield from Geant4 compared to the rest of the codes. For the deuteron induced reactions, a similar trend is seen at low incident ion energies, with high variations between the codes visible in this plot. At higher E_i, there is minimal variation between the codes, with the shape of the spectra and neutron yields in each bin being similar across all codes in this energy range.

4.5. *Computational performance*

The choice of simulation code for particle transport is often not only influenced by its accuracy, but also by its computational performance, particularly in scenarios where computing resources are limited. Fig. 20 presents a visual representation of the single-threaded throughput (number of particles simulated per second) for each simulation code for the reactions of interest. The computational configuration used for these performance tests is described in Section 3.4. For each reaction, the box plot depicts the distribution of throughput values calculated across the range of simulated incident energies. This metric is useful for evaluating the baseline computational efficiency of each code, independent of any parallelisation, and offers practical insight into relative computational cost and scalability. In large-scale simulation studies, faster throughput can translate to shorter runtimes, reduced energy consumption and more effective use of computational resources.

Across all the evaluated reactions, PHITS exhibits the highest single-thread throughput compared to Geant4, MCNP and FLUKA. In all cases, the simulation performed with PHITS is completed in less than one sixth of the time needed by the other codes. The spread of the throughputs associated with each code in Fig. 20 is due to the difference in computation time across the range of energies simulation. A breakdown of the speeds observed at each energy is presented in Supplementary Material Section S2.6. As a general trend, higher E_i energies take increased times to run compared to lower energies across all codes and reactions. The spread observed for FLUKA and MCNP is relatively narrow compared to that of Geant4 and PHITS. This suggests that FLUKA and MCNP exhibit consistent performance across a wider incident energy range, while Geant4 and PHITS computation times are heavily dependent on the E_i energy chosen. Because computational performance is only one aspect of overall code performance, it is recommended that throughput speeds are considered alongside each code's agreement with experimental data when making an informed judgement on which Monte Carlo code to adopt for a given application.

Since each event in a Monte Carlo simulation is independent from the others, running multiple threads or processes in parallel is expected to increase overall throughput almost linearly. Multi-threading is generally preferable to multi-process simulations since it allows data structures to be shared in memory with minimal overhead, although on modern operating systems using copy-on-write memory this distinction is minor in practice. Future work may involve comparing computational speeds of each code (except FLUKA, since it cannot presently run in multi-threaded mode) across increasing numbers of threads on a multi-core CPU.

5. Conclusion

In this work, the Geant4 11.1.3, PHITS 3.33, MCNP 6.3 and FLUKA 4-4.0 Monte Carlo codes have been benchmarked for the modelling of several low-energy neutron production target reactions which have been proposed for use in accelerator-based neutron sources. All simulations were performed using developer recommended configurations for each code, with the associated physics models and cross section data libraries relevant to the evaluated reactions. Available published experimental data for neutron yield (total yield, yield at 0°), angular neutron yield, and neutron spectra were collated and compared to simulation results from each code.

Compared to available experimental datasets, Geant4, PHITS and MCNP show the best performance for the ^{9}Be(p,n)^{9}B reaction in reproducing total and forward-directed neutron yield, with PHITS showing the best agreement on energy spectra across 5–9 MeV incident protons. For ^{7}Li(p,n)^{7}Be, FLUKA and PHITS provide the closest yield to experiment, while all codes reproduce the 1.91 MeV spectrum well. For the deuteron-induced reactions, Geant4, MCNP and PHITS outperform FLUKA for neutron yield. For higher incident ion energies (above ~6 MeV), all codes predict spectral shape well. All codes produce similar errors compared to available experimental results, with the exception of FLUKA in providing higher error for some cases. Additional tests comparing the computational performance (particles/s) of each code show that PHITS currently provides the highest single-threaded computational throughput for all reactions.

This study shows that there is a range of variation in yield between all the codes for the simulation of each reaction depending on the incident ion energy (E_i), emission angle, and emitted neutron energy. No single Monte Carlo code consistently outperforms the others in terms of providing the best match with experimental data across all reaction channels. Each code typically exhibits particular ranges of emission angle or neutron energy for which there are both high and low levels of agreement with available experimental data. Therefore, the choice of code for any given simulation should be made on the basis of the specific reaction of interest and the required neutron emission (yield, spectral and angular distribution) characteristics.

For this benchmark study, we intentionally used each code's developer-recommended physics and cross-section data libraries so that the results reflect baseline predictive capability rather than that from optimised configurations. Future studies may extend beyond the baseline developer-recommended Monte Carlo code configurations to compare the performance of different cross-section databases within individual codes. A key prerequisite, however, is high quality experimental reference data. Most published datasets have not been produced recently (within the last 20 years), cover only select energies or emission angles relevant to ABNS design, and have not been independently replicated. By collating and consolidating these experimental datasets, this work provides an immediate resource and reference point for future benchmarking and library development. It is essential that there is focus on repeating, extending and updating the available experimental datasets to provide more robust reference data. As these datasets are often used for validating and improving cross-section data libraries for Monte Carlo codes, addressing these gaps is crucial for enhancing the reliability of future simulation platforms.

CRediT authorship contribution statement

Sherryn MacLeod: Writing – review & editing, Writing – original draft, Visualization, Validation, Software, Resources, Project administration, Methodology, Investigation, Funding acquisition, Formal analysis, Data curation, Conceptualization; **Klaudiusz Jakubowski:** Writing – review & editing, Methodology, Conceptualization; **James Vohradsky:** Software, Investigation; **Daniel R. Franklin:** Writing – review & editing; **Toshiro Sakabe:** Writing – review & editing, Validation, Investigation; **Akram Hamato:** Software; **Masahiro Okamura:** Writing – review & editing, Supervision, Resources, Methodology, Funding acquisition, Conceptualization; **Susanna Guatelli:** Writing – review & editing, Validation, Supervision, Software, Resources, Methodology, Funding acquisition, Conceptualization; **Mitra Safavi-Naeini:** Writing – review & editing, Supervision, Resources, Project administration, Methodology, Funding acquisition, Conceptualization.

Data availability

The raw data for all simulations conducted during this study is available at https://drive.google.com/drive/folders/1-ajy4LfnzONme_9gi9SHesx7KHy7XKYF?usp=drive_link. Monte Carlo simulation input code and post-processing scripts are available from the corresponding author on reasonable request.

Declaration of competing interest

The authors declare that they have no known competing financial interests or personal relationships that could have appeared to influence the work reported in this paper.

Acknowledgements

This research was supported by an Australian Government Research Training Scholarship and an Australian Institute of Nuclear Science and Engineering (AINSE) Ltd. Residential Student Scholarship (RSS). The bulk of simulations were performed using the high-performance computing resources granted through the National Computational Merit Allocation Scheme (NCMAS) on the Gadi facility at the National Computational Infrastructure (NCI).

Supplementary material

Supplementary material associated with this article can be found in the online version at 10.1016/j.cpc.2025.109998.

References

[1] Y. Kiyanagi, Y. Sakurai, H. Kumada, H. Tanaka, Status of accelerator-based BNCT projects worldwide, AIP Conference Proceedings, American Institute of Physics Inc., 2019. vol. 2160, p. 050012. https://doi.org/10.1063/1.5127704.

[2] Y. Xiao, Z. Chen, Y. Yang, X. Wang, Development progress of the neutron imaging station in CPHS, Phys. Procedia 69 (2015) 96–103. https://doi.org/10.1016/j.phpro.2015.07.014.

[3] Y. Kiyanagi, Neutron imaging at compact accelerator-driven neutron sources in Japan, J. Imaging 4 (2018) 55. https://doi.org/10.3390/jimaging4040055.

[4] C. Andreani, I.S. Anderson, J.M. Carpenter, G. Festa, G. Gorini, C.-K. Loong, R. Senesi, Applications of compact accelerator-driven neutron sources: an updated assessment from the perspective of materials research in Italy, Phys. Procedia 60 (2014) 228–237. https://doi.org/10.1016/j.phpro.2014.11.032.

[5] X. Li, T. Jiao, W. Li, Q. Zheng, N. Ni, S. Zhao, S. Zhao, F. Cheng, L. Yang, H. Yu, Spectrum measurement of secondary neutron induced by 9Be (p, n) reaction in low-Earth orbit 1047 (2023) 167783. https://doi.org/10.1016/j.nima.2022.167783.

[6] Y. Wang, D. Chen, R.S. Augusto, J. Liang, Z. Qin, J. Liu, Z. Liu, Production review of accelerator-based medical isotopes, Molecules 27 (2022) 5294. https://doi.org/10.3390/molecules27165294.

[7] S.A. Hoedl, W.D. Updegraff, The production of medical isotopes without nuclear reactors or uranium enrichment, Sci. Glob. Secur. 23 (2015) 121–153. https://doi.org/10.1080/08929882.2015.1037123.

[8] S. Taskaev, T. Bykov, D. Kasatov, I. Kolesnikov, A. Koshkarev, A. Makarov, S. Savinov, I. Shchudlo, E. Sokolova, Measurement of the 7Li $(p, p'\gamma)$ 7Li reaction cross-section and 478 keV photon yield from a thick lithium target at proton energies from 0.65 MeV to 2.225 MeV, Nucl. Instrum. Methods Phys. Res. Sect. B 502 (2021) 85–94. https://doi.org/10.1016/j.nimb.2021.06.010.

[9] Z. Zhang, Y. Chong, Y. Liu, J. Pan, C. Huang, Q. Sun, Z. Liu, X. Zhu, Y. Shao, C. Jin, T. Liu, A review of planned, ongoing clinical studies and recent development of BNCT in Mainland of China, Cancers 15 (2023) 4060. https://doi.org/10.3390/cancers15164060

[10] I.A.E. Agency, Current status of neutron capture therapy, International Atomic Energy Agency, 2001

[11] H. Kumada, T. Sakae, H. Sakurai, Current development status of accelerator-based neutron source for boron neutron capture therapy, EPJ Tech. Instrum. 10 (2023) 18. https://doi.org/10.1140/epjti/s40485-023-00105-5

[12] D.E. Cartelli, M.E. Capoulat, M. Baldo, J.C.S. Sandín, M. Igarzabal, M.F.D. Grosso, A.A. Valda, N. Canepa, M. Gun, D.M. Minsky, Status of low-energy accelerator-based BNCT worldwide and in Argentina Appl. Radiat. Isot. 166 (2020) 109315. https://doi.org/10.1016/j.apradiso.2020.109315.

[13] F.J. Bermejo, F. Sordo, Chapter 2—Neutron sources, in: F. Fernandez-Alonso, D.L. Price, (Eds.), Experimental Methods in the Physical Sciences, volume 44 of Neutron Scattering - Fundamentals, Academic Press, 2013, pp. 137–243 https://doi.org/10.1016/B978-0-12-398374-9.00002-4

[14] D.L. Chichester, Production and applications of neutrons using particle accelerators, in: Industrial Accelerators and Their Applications, World Scientific, 2012, pp. 243–305.

[15] M.E. Capoulat, N. Sauzet, A.A. Valda, L. Gagetti, O. Guillaudin, L. Lebreton, D. Maire, P. Mastinu, J. Praena, Q. Riffard, Neutron spectrometry of the 9Be (d (1.45 MeV), n) 10B reaction for accelerator-based BNCT. Nucl. Instrum. Methods Phys. Res. Sect. B 445 (2019) 57–62.

[16] A.A. Bertolo, A. Cánneva, J.A. Donadelli, P.A. Gaviola, A.J. Kreiner, M.F.D. Grosso, Manufacture, characterization and proton irradiation effects of ^{12}C and ^{13}C thick targets, J. Mater. Sci. 56 (2021) 6997–7007. https://doi.org/10.1007/s10853-020-05728-7

[17] Y. Kiyanagi, Neutron applications developing at compact accelerator-driven neutron sources, AAPPS Bull. 31 (2021) 22. https://doi.org/10.1007/s43673-021-00022-3

[18] S. Halfon, M. Paul, A. Arenshtam, D. Berkovits, D. Cohen, I. Eliyahu, D. Kijel, I. Mardor, I. Silverman, High-power electron beam tests of a liquid-lithium target and characterization study of 7Li(p,n) near-threshold neutrons for accelerator-based boron neutron capture therapy, Appl. Radiat. Isot. 88, 2014 238–242. Elsevier Ltd. https://doi.org/10.1016/j.apradiso.2013.11.043

[19] T. Kobayashi, K. Miura, N. Hayashizaki, M. Aritomi, Development of liquid-lithium film jet-flow for the target of 7Li (p, n) 7Be reactions for BNCT, Appl. Radiat. Isot. 88 (2014) 198–202. https://doi.org/10.1016/j.apradiso.2013.12.013.

[20] B. Bayanov, V. Belov, V. Kindyuk, E. Oparin, S. Taskaev, Lithium neutron producing target for BINP accelerator-based neutron source, Appl. Radiat. Isot. 61 (2004) 817–821. https://doi.org/10.1016/j.apradiso.2004.05.032.

[21] H. Kumada, F. Naito, K. Hasegawa, H. Kobayashi, T. Kurihara, K. Takada, T. Onishi, H. Sakurai, A. Matsumura, T. Sakae, Development of LINAC-based neutron source for boron neutron capture therapy in university of Tsukuba, Plasma Fusion Res. 13, 2018, Japan Society of Plasma Science and Nuclear Fusion Research. https://doi.org/10.1585/pfr.13.2406006

[22] B. Bayanov, V. Belov, S. Taskaev, Neutron producing target for accelerator based neutron capture therapy, in: Journal of Physics: Conference Series vol. 41, IOP Publishing, 2006, p. 460. https://doi.org/10.1088/1742-6596/41/1/051.

[23] Z. Qiao, X. Li, Y. Lv, Y. Xie, Y. Hu, J. Wang, H. Li, S. Wang, Depositing a titanium coating on the lithium neutron production target by magnetron sputtering technology, Materials 14 (2021) 1873. https://doi.org/10.3390/ma14081873.

[24] S.Y. Taskaev, Accelerator based epithermal neutron source, Phys. Part. Nucl. 46 (2015) 956–990. https://doi.org/10.1134/S1063779615060064.

[25] H. Kumada, T. Kurihara, M. Yoshioka, H. Kobayashi, H. Matsumoto, T. Sugano, H. Sakurai, T. Sakae, A. Matsumura, Development of beryllium-based neutron target system with three-layer structure for accelerator-based neutron source for boron neutron capture therapy, Appl. Radiat. Isot. 106, 2015 78–83, Elsevier Ltd. https://doi.org/10.1016/j.apradiso.2015.07.033

[26] T.E. Blue, J.C. Yanch, Accelerator-based epithermal neutron sources for boron neutron capture therapy of brain tumors, J. Neurooncol. 62 (2003) 19–31. https://doi.org/10.1007/BF02699931.

[27] M.E. Capoulat, A.J. Kreiner, A 13C(d,n)-based epithermal neutron source for boron neutron capture therapy, Assoc. Ital. Fis. Med. 33 (2017) 106–113. https://doi.org/10.1016/j.ejmp.2016.12.017

[28] H. Takeshita, Y. Watanabe, K. Nakano, S. Manabe, K. Aoki, N. Araki, K. Yoshinami, T. Kin, N. Shigyo, J. Koga, S. Makise, T. Yoshioka, M. Tanaka, T. Teranishi, Neutron production from thick LiF, C, Si, Ni, Mo, and Ta targets bombarded by 13.4-MeV deuterons, EPJ Web Conf. 239 2020 01018. https://doi.org/10.1051/epjconf/202023901018

[29] A.J. Kreiner, J. Bergueiro, D. Cartelli, M. Baldo, W. Castell, J.G. Asoia, J. Padulo, J.C.S. Sandín, M. Igarzabal, J. Erhardt, D. Mercuri, A.A. Valda, D.M. Minsky, M.E. Debray, H.R. Somacal, M.E. Capoulat, M.S. Herrera, M.F.D. Grosso, L. Gagetti, M.S. Anzorena, N. Canepa, N. Real, M. Gun, H. Tacca, Present status of accelerator-based BNCT, Rep. Pract. Oncol. Radiother. 21, Urban and Partner, 2016 95–101. https://doi.org/10.1016/j.rpor.2014.11.004

[30] M.E. Capoulat, D.M. Minsky, A.J. Kreiner, Computational assessment of deep-seated tumor treatment capability of the 9Be(d,n)10B reaction for accelerator-based boron neutron capture therapy (AB-BNCT), Phys. Med. 30 (2014) 133–146. https://doi.org/10.1016/j.ejmp.2013.07.001

[31] G. Lhersonneau, T. Malkiewicz, D. Vakhtin, V. Plokhoi, O. Alyakrinskiy, M. Cinausero, Y. Kandiev, H. Kettunen, S. Khlebnikov, H. Penttilä, G. Prete, V. Rizzi, S. Samarin, L. Tecchio, W.H. Trzaska, G. Tyurin, Neutron yield from a 13C thick target irradiated by protons of intermediate energy, Nucl. Instrum. Methods Phys. Res., Sect. A 576 (2007) 371–379. https://doi.org/10.1016/j.nima.2007.02.106

[32] S. Agostinelli, J. Allison, K. Amako, J. Apostolakis, H. Araujo, P. Arce, M. Asai, D. Axen, S. Banerjee, G. Barrand, F. Behner, L. Bellagamba, J. Boudreau, L. Broglia, A. Brunengo, H. Burkhardt, S. Chauvie, J. Chuma, R. Chytracek, G. Cooperman, G. Cosmo, P. Degtyarenko, A. Dell'acqua, G. Depaola, D. Dietrich, R. Enami, A. Feliciello, C. Ferguson, H. Fesefeldt, G. Folger, F. Foppiano, A. Forti, S. Garelli, S. Giani, R. Giannitrapani, D. Gibin, J.J.G. Cadenas, I. González, G.G. Abril, G. Greeniaus, W. Greiner, V. Grichine, A. Grossheim, S. Guatelli, P. Gumplinger, R. Hamatsu, K. Hashimoto, H. Hasui, A. Heikkinen, A. Howard, V. Ivanchenko, A. Johnson, F.W. Jones, J. Kallenbach, N. Kanaya, M. Kawabata, Y. Kawabata, M. Kawaguti, S. Kelner, P. Kent, A. Kimura, T. Kodama, R. Kokoulin, M. Kossov, H. Kurashige, E. Lamanna, T. Lampén, V. Lara, V. Lefebure, F. Lei, M. Liendl, W. Lockman, F. Longo, S. Magni, M. Maire, E. Medernach, K. Minamimoto, P.M.D. Freitas, Y. Morita, K. Murakami, M. Nagamatu, R. Nartallo, P. Nieminen, T. Nishimura, K. Ohtsubo, M. Okamura, S. O'neale, Y. Oohata, K. Paech, J. Perl, A. Pfeiffer, M.G. Pia, F. Ranjard, A. Rybin, S. Sadilov, E. Di Salvo, G. Santin, T. Sasaki, N. Savvas, Y. Sawada, S. Scherer, S. Sei, V. Sirotenko, D. Smith, N. Starkov, H. Stoecker, J. Sulkimo, M. Takahata, S. Tanaka, E. Tcherniaev, E. Safai Tehrani, M. Tropeano, P. Truscott, H. Uno, L. Urban, P. Urban, M. Verderi, A. Walkden, W. Wander, H. Weber, J.P. Wellisch, T. Wenaus, D.C. Williams, D. Wright, T. Yamada, H. Yoshida, D. Zschiesche, Geant4—a simulation toolkit. Nucl. Instrum. Methods Phys. Res., Sect. A 506 (2003) 250–303. https://doi.org/10.1016/S0168-9002(03)01368-8

[33] P. Arce, D. Bolst, M.-C. Bordage, J.M.C. Brown, P. Cirrone, M.A. Cortés-Giraldo, D. Cutajar, G. Cuttone, L. Desorgher, P. Dondero, A. Dotti, B. Faddegon, C. Fedon, S. Guatelli, S. Incerti, V. Ivanchenko, D. Konstantinov, I. Kyriakou, G. Latyshev, A. Le, C. Mancini-Terracciano, M. Maire, A. Mantero, M. Novak, C. Omachi, L. Pandola, A. Perales, Y. Perrot, G. Petringa, J.M. Quesada, J. Ramos-Méndez, F. Romano, A.B. Rosenfeld, L.G. Sarmiento, D. Sakata, T. Sasaki, I. Sechopoulos, E.C. Simpson, T. Toshito, D.H. Wright, Report on G4-Med, a Geant4 benchmarking system for medical physics applications developed by the Geant4 medical simulation benchmarking group. Med. Phys. 48 (2021) 19–56. https://doi.org/10.1002/mp.14226

[34] J.A. Kulesza, T.R. Adams, J.C. Armstrong, S.R. Bolding, F.B. Brown, J.S. Bull, T.P. Burke, A.R. Clark, R.A.A. III Forster, J.F. Giron, T.S. Grieve, C.J. Josey, R.L. Martz, G.W. Mckinney, E.J. Pearson, M.E. Rising, C.J.C. Jr. Solomon, S. Swaminarayan, T.J. Trahan, S.C. Wilson, A.J. Zukaitis, MCNP®Code Version 6.3.0 Theory & User Manual, Technical Report LA-UR-22-30006, Los Alamos National Laboratory (LANL), Los Alamos, NM (United States), (2022) https://doi.org/10.2172/1889957

[35] M.E. Rising, J.C. Armstrong, S.R. Bolding, F.B. Brown, J.S. Bull, T.P. Burke, A.R. Clark, D.A. Dixon, R.A. III Forster, J.F. Giron, T.S. Grieve, H.G. III Hughes, C.J. Josey, J.A. Kulesza, R.L. Martz, A.P. Mccartney, G.W. Mckinney, S.W. Mosher, E.J. Pearson, C.J. Jr. Solomon, S. Swaminarayan, J.E. Sweezy, S.C. Wilson, A.J. Zukaitis, MCNP®Code V.6.3.0 Release Notes, Technical Report LA-UR-22-33103, Los Alamos National Laboratory (LANL), Los Alamos, NM (United States), (2023) https://doi.org/10.2172/1909545

[36] T. Sato, Y. Iwamoto, S. Hashimoto, T. Ogawa, T. Furuta, S.-I. Abe, T. Kai, Y. Matsuya, N. Matsuda, Y. Hirata, T. Sekikawa, L. Yao, P.-E. Tsai, H.N. Ratliff, H. Iwase, Y. Sakaki, K. Sugihara, N. Shigyo, L. Sihver, K. Niita, Recent improvements of the particle and heavy ion transport code system - PHITS version 3, J. Nucl. Sci. Technol. 33 (2024) 127–135. https://doi.org/10.1080/00223131.2023.2275736

[37] C. Ahdida, D. Bozzato, D. Calzolari, F. Cerutti, N. Charitonidis, A. Cimmino, A. Coronetti, G.L. D'alessandro, A.D. Servelle, L.S. Esposito, R. Froeschl, R.G. Alía, A. Gerbershagen, S. Gilardoni, D. Horváth, G. Hugo, A. Infantino, V. Kouskoura, A. Lechner, B. Lefebvre, G. Lerner, M. Magistris, A. Manousos, G. Moryc, F.O. Ruiz, F. Pozzi, D. Prelipcean, S. Roesler, R. Rossi, M.S. Gilarte, FS. Pujol, P. Schoofs, V. Stránský, C. Theis, A. Tsinganis, R. Versaci, V. Vlachoudis, A. Waets, M. Widorski, New capabilities of the FLUKA multi-purpose code. Front. Phys. 9 (2022). https://doi.org/10.3389/fphy.2021.788253

[38] G. Battistoni, T. Boehlen, F. Cerutti, P.W. Chin, L.S. Esposito, A. Fassò, A. Ferrari, A. Lechner, A. Empl, A. Mairani, A. Mereghetti, P.G. Ortega, J. Ranft, S. Roesler, P.R. Sala, V. Vlachoudis, G. Smirnov, Overview of the FLUKA code. Ann. Nucl. Energy 82 (2015) 10–18. https://doi.org/10.1016/j.anucene.2014.11.007

[39] A. Koning, S. Hilaire, S. Goriely, TALYS: modeling of nuclear reactions, Eur. Phys. J. A 59, Springer, Berlin Heidelberg, 2023 131. https://doi.org/10.1140/epja/s10050-023-01034-3

[40] A.J. Koning, D. Rochman, J.C. Sublet, N. Dzysiuk, M. Fleming, S.V.D. Marck, TENDL: complete nuclear data library for innovative nuclear science and technology, Nucl. Data Sheets 155 (2019) 1–55. https://doi.org/10.1016/j.nds.2019.01.002

[41] S. Nakayama, O. Iwamoto, Y. Watanabe, K. Ogata, JENDL/DEU-2020: deuteron nuclear data library for design studies of accelerator-based neutron sources, J. Nucl. Sci. Technol. 58 (2021) 805–821. https://doi.org/10.1080/00223131.2020.1870010

[42] A.J.M. Plompen, O. Cabellos, C.D.S. Jean, M. Fleming, A. Algora, M. Angelone, P. Archier, E. Bauge, O. Bersillon, A. Blokhin, F. Cantargi, A. Chebboubi, C. Diez, H. Duarte, E. Dupont, J. Dyrda, B. Erasmus, L. Fiorito, U. Fischer, D. Flammini, D. Foligno, M.R. Gilbert, J.R. Granada, W. Haeck, F.-J. Hambsch, P. Helgesson, S. Hilaire, I. Hill, M. Hursin, R. Ichou, R. Jacqmin, B. Jansky, C. Jouanne, M.A. Kellett, D.H. Kim, H.I. Kim, I. Kodeli, A.J. Koning, A.Y. Konobeyev, S. Kopecky, B. Kos, A. Krása, L.C. Leal, N. Leclaire, P. Leconte, Y.O. Lee, H. Leeb, O. Litaize, M. Majerle, J.I.M. Damián, F. Michel-Sendis, R.W. Mills, B. Morillon, G. Noguère, M. Pecchia, S. Pelloni, P. Pereslavtsev, R.J. Perry, D. Rochman, A. Röhrmoser, P. Romain, P. Romojaro, D. Roubtsov, P. Sauvan, P. Schillebeeckx, K.H. Schmidt, O. Serot, S. Simakov, I. Sirakov, H. Sjöstrand, A. Stankovskiy, J.C. Sublet, P. Tamagno, A. Trkov, S.V.D. Marck, F. Álvarez Velarde, R. Villari, T.C. Ware, K. Yokoyama, G. Žerovnik, The joint evaluated fission and fusion nuclear data library, JEFF-3.3, Eur. Phys. J. A 56 (2020) 181. https://doi.org/10.1140/epja/s10050-020-00141-9

[43] O. Iwamoto, N. Iwamoto, S. Kunieda, F. Minato, S. Nakayama, Y. Abe, K. Tsubakihara, S. Okumura, C. Ishizuka, T. Yoshida, S. Chiba, N. Otuka, J.-C. Sublet, H. Iwamoto, K. Yamamoto, Y. Nagaya, K. Tada, C. Konno, N. Matsuda, K. Yokoyama, H. Taninaka, A. Oizumi, M. Fukushima, S. Okita, G. Chiba, S. Sato, M. Ohta, S. Kwon, Japanese evaluated nuclear data library version 5: JENDL-5, J. Nucl. Sci. Technol. 60 (2023) 1–60. https://doi.org/10.1080/00223131.2022.2141903

[44] H.R. Trellue, R.C. Little, M.C. White, R.E. Macfarlane, A.C. Kahler, A continuous-energy MCNP neutron data library based on ENDF/B-VII.0, Nucl. Technol. 168, (2009) 832–836.

[45] M. Chadwick, M. Herman, P. Obložinský, M. Dunn, Y. Danon, A. Kahler, D. Smith, B. Pritychenko, G. Arbanas, R. Arcilla, R. Brewer, D. Brown, R. Capote, A. Carlson, Y. Cho, H. Derrien, K. Guber, G. Hale, S. Hoblit, S. Holloway, T. Johnson, T. Kawano, B. Kiedrowski, H. Kim, S. Kunieda, N. Larson, L. Leal, J. Lestone, R. Little, E. Mccutchan, R. Macfarlane, M. Macinnes, C. Mattoon, R. Mcknight, S. Mughabghab, G. Nobre, G. Palmiotti, A. Palumbo, M. Pigni, V. Pronyaev, R. Sayer, A. Sonzogni, N. Summers, P. Talou, I. Thompson, A. Trkov, R. Vogt, S.V.D. Marck, A. Wallner, M. White, D. Wiarda, P. Young, ENDF/B-VII.1 nuclear data for science and technology: cross sections, covariances, fission product yields and decay data, Nucl. Data Sheets 112 (2011) 2887–2996. https://doi.org/10.1016/j.nds.2011.11.002

[46] J.L. Conlin, S.J. Gardiner, D.K. Parsons, A.C. Kahler, B. Lee, M.C. White, Release of ENDF/B-VII. 1-based Continuous Energy Neutron Cross Section Data Tables for MCNP, Transactions of the American Nuclear Socity, LA-UR-13-20240, American Nuclear Society, Atlanta, Georgia, 2013.

[47] D.K. Parsons, J.L. Conlin, Release of Continuous Representation for S (α, β) ACE Data, LA-UR-14-21878, Los Alamos Nat. Lab., Los Alamos, NM, USA, Tech. Rep., 2014.

[48] N. Otuka, E. Dupont, V. Semkova, B. Pritychenko, A.I. Blokhin, M. Aikawa, S. Babykina, M. Bossant, G. Chen, S. Dunaeva, R.A. Forrest, T. Fukahori, N. Furutachi, S. Ganesan, Z. Ge, O.O. Gritzay, M. Herman, S. Hlavač, K. Katō, B. Lalremruata, Y.O. Lee, A. Makinaga, K. Matsumoto, M. Mikhaylyukova, G. Pikulina, V.G. Pronyaev, A. Saxena, O. Schwerer, S.P. Simakov, N. Soppera, R. Suzuki, S. Takács, X. Tao, S. Taova, F. Tárkányi, V.V. Varlamov, J. Wang, S.C. Yang, V. Zerkin, Y. Zhuang, Towards a more complete and accurate experimental nuclear reaction data library (EXFOR): international collaboration between nuclear reaction data centres (NRDC), Nucl. Data Sheets 120 (2014) 272–276. https://doi.org/10.1016/j.nds.2014.07.065

[49] N. Otuka, N. Soppera, How to search on EXFOR, J. Phys. Conf. Ser. 1555 (2020) 12009. https://doi.org/10.1088/1742-6596/1555/1/012009

[50] M. Hawkesworth, Neutron radiography equipment and methods. Atom. Energy Rev. 15 (1977) 169–220. .

[51] L.D. Stephens, A.J. Miller, Radiation studies at a medium energy accelerator, in: 2nd International Conference on Accelerator Dosimetry and Experience, California, 1969.

[52] M.A. Atta, M.C. Scott, The neutron yield from Li, Be, Co and Cu under proton bombardment at energies from 5 to 10 MeV, J. Nucl. Eng. 27 (1973) 875–884. https://doi.org/10.1016/0022-3107(73)90032-4

[53] A.A. Lychagin, B.V. Zhuravlev, V.G. Demenkov, U.A. Tchalyi, Measurement of energy spectra and angular distributions of the thick target 9 Be (p,n) neutrons, in: Conf: Int. Sem. on Interactions of Neutrons with Nuclei, (2003) p. 333.

[54] G. Yue, J. Chen, R. Song, Study of boron neutron capture therapy used neutron source with protons bombarding a thick 9Be target, Med. Phys. 24 (1997) 851–855. https://doi.org/10.1118/1.597984

[55] W.B. Howard, S.M. Grimes, T.N. Massey, S.I. Al-Quraishi, D.K. Jacobs, C.E. Brient, J.C. Yanch, Measurement of the thick-target 9Be (p, n) neutron energy spectra. Nucl. Sci. Eng. 138 (2001) 145–160.

[56] H.J. Brede, G. Dietze, K. Kudo, U.J. Schrewe, F. Tancu, C. Wen, Neutron yields from thick Be targets bombarded with deuterons or protons, Nucl. Instrum. Methods Phys. Res., Sect. A 274 (1989) 332–344. https://doi.org/10.1016/0168-9002(89)90399-9

[57] M.A. Lone, C.B. Bigham, J.S. Fraser, H.R. Schneider, T.K. Alexander, A.J. Ferguson, A.B. Mcdonald, Thick target neutron yields and spectral distributions from the 7Li(pd, n) and 9Be(pd, n) reactions. Nucl. Instrum. Methods 143 (1977) 331–344. https://doi.org/10.1016/0029-554X(77)90616-4

[58] G. Martín-Hernández, P. Mastinu, E. Musacchio-Gonzalez, R. Capote, H. Lubián, M.M. Martinez, Li 7 (p,n) Be 7 cross section from threshold to 1960 keV and precise measurement of the Au 197 (n,γ) spectrum-averaged cross section at 30 keV, Phys. Rev. C 7 (2019) 99. https://doi.org/10.1103/PhysRevC.99.034616

[59] M.C. Scott, The rate of energy loss and neutron yield for protons on thick lithium targets at energies from 3 to 10 MeV, J. Nucl. Eng. 25 (1971) 405–416. https://doi.org/10.1016/0022-3107(71)90077-3

[60] C.L. Lee, X.L. Zhou, Thick target neutron yields for the 7Li(p,n)7Be reaction near threshold, Nucl. Instrum. Methods Phys. Res. Sect. B 152 (1999) 1–11. https://doi.org/10.1016/S0168-583X(99)00026-9

[61] V.N. Kononov, M.V. Bokhovko, O.E. Kononov, N.A. Soloviev, W.T. Chu, D. Nigg, Accelerator-based fast neutron sources for neutron therapy, Nucl. Instrum. Methods Phys. Res., Sect. A 564 (2006) 525–531. https://doi.org/10.1016/j.nima.2006.03.043

[62] W. Yu, G. Yue, X. Han, J. Chen, B. Tian, Measurements of the neutron yields from reaction (thick target) with incident energies from 1.885 to 2.0 MeV, Med. Phys. 25 (1998) 1222–1224. https://doi.org/10.1118/1.598299

[63] Y. Zuo, G. Tang, Z. Guo, J. Guo, Y. Pei, J. Xu, H. Wang, Y. Lu, Neutron yields of thick Be target bombarded with low energy deuterons, Phys. Procedia 60 (2014) 220–227. https://doi.org/10.1016/j.phpro.2014.11.031

[64] J.W. Meadows, The 9Be(d, n) thick-target neutron spectra for deuteron energies between 2.6 and 7.0 MeV, Nucl. Instrum. Methods Phys. Res., Sect. A 324 (1993) 239–246. https://doi.org/10.1016/0168-9002(93)90983-O

[65] K.A. Weaver, J.D. Anderson, H.H. Barschall, J.C. Davis, L. Be, C. Nuclear, Neutron spectra from deuteron bombardment of D, Li, Be, and C. Nucl. Sci. Eng. 52 (1973) 35–45. https://doi.org/10.13182/NSE73-A23287

[66] Y. Tajiri, Y. Watanabe, N. Shigyo, K. Hirabayashi, T. Nishizawa, K. Sagara, Measurement of double differential neutron yields from thick carbon target irradiated by 5-MeV and 9-MeV deuterons. Prog. Nucl. Sci. Technol. 4 (2014) 582–586.

[67] N. Colonna, L. Beaulieu, L. Phair, G.J. Wozniak, L.G. Moretto, W.T. Chu, B.A. Ludewigt, Measurements of low-energy (d,n) reactions for BNCT, Med. Phys. 26 (1999) 793–798. https://doi.org/10.1118/1.598599

[68] M.K.A. Patwary, T. Kin, K. Aoki, K. Yoshinami, M. Yamaguchi, Y. Watanabe, K. Tsukada, N. Sato, M. Asai, T.K. Sato, Y. Hatsukawa, S. Nakayama, Measurement of double-differential thick-target neutron yields of the C(d,n) reaction at 12, 20, and 30 MeV, J. Nucl. Sci. Technol. 58 (2021) 252–258. https://doi.org/10.1080/00223131.2020.1819908

[69] J.P. Meulders, P. Leleux, P.C. Macq, C. Pirart, Fast neutron yields and spectra from targets of varying atomic number bombarded with deuterons from 16 to 50 MeV, Phys. Med. Biol. 20 (1975) 235–243. https://doi.org/10.1088/0031-9155/20/2/005

[70] S. Agosteo, P. Colautti, J. Esposito, A. Fazzi, M.V. Introini, A. Pola, Characterization of the energy distribution of neutrons generated by 5 MeV protons on a thick beryllium target at different emission angles, Appl. Radiat. Isot. 69 (2011) 1664–1667. https://doi.org/10.1016/j.apradiso.2011.03.015

[71] S. Kunieda, K. Yamamoto, C. Konno, Y. Iwamoto, O. Iwamoto, Y. Wakabayashi, Y. Ikeda, Estimation of double-differential cross-sections of 9Be(p,xn) reaction for new nuclear data library JENDL-5, J. Neutron Res. 24 (2023) 329–335. https://doi.org/10.3233/JNR-220019

[72] W. Ratynski, F. Käppeler, Neutron capture cross section of Au 197: a standard for stellar nucleosynthesis, Phys. Rev. C 37 (1988) 595–604. https://doi.org/10.1103/PhysRevC.37.595

[73] C. Lederer, F. Käppeler, M. Mosconi, R. Nolte, M. Heil, R. Reifarth, S. Schmidt, I. Dillmann, U. Giesen, A. Mengoni, A. Wallner, Definition of a standard neutron field with the 7 Li(p,n)7 Be reaction, Phys. Rev. C 85 (2012) 55809. https://doi.org/10.1103/PhysRevC.85.055809

[74] G. Feinberg, M. Friedman, A. Krása, A. Shor, Y. Eisen, D. Berkovits, D. Cohen, G. Giorginis, T. Hirsh, M. Paul, A.J.M. Plompen, E. Tsuk, Quasi-stellar neutrons from the 7 Li(p,n)7 Be reaction with an energy-broadened proton beam, Phys. Rev. C 85 (2012) 55810. https://doi.org/10.1103/PhysRevC.85.055810

[75] J. Guzek, U.A.S. Tapper, W.R. Mcmurray, J.I.W. Watterson, Characterization of the 9Be(d,n)10B reaction as a source of neutrons employing commercially available radio frequency quadrupole (RFQ) linacs, in: International Conference Neutrons in Research and Industry 2867, SPIE, 1997, pp. 509–512 . https://doi.org/10.1117/12.267963

[76] D. Smith, J. Meadows, P. Guenther, Fast-neutron-spectrum measurements for the thick-target 9Be(d,n)10B reaction at E/sub d/ = 7 MeV, Technical Report, Argonne National Laboratory, United States, (1985). ANL/NDM-90 INIS Reference Number: 16076620.